Tectonics®

RESEARCH ARTICLE
10.1029/2020TC006431

Key Points:

- Voluminous two-mica granite emplacement in the Anaconda metamorphic core complex (AMCC) footwall occurred in the Paleocene, at least 3 Myr before the onset of extension
- Zircon (U-Th)/He cooling ages ranging from ~48 to 25 Ma provide new timing constraints on footwall exhumation in the AMCC
- εHf trends in the AMCC footwall rocks and Idaho batholith reflect increased mantle input in the Eocene due to the removal of the subducted Farallon slab

Supporting Information:

Supporting Information may be found in the online version of this article.

Correspondence to:

C. J. Howlett,
cadenhowlett@email.arizona.edu

Citation:

Howlett, C. J., Reynolds, A. N., & Laskowski, A. K. (2021). Magmatism and extension in the Anaconda metamorphic core complex of western Montana and relation to regional tectonics. *Tectonics*, *40*, e2020TC006431. https://doi.org/10.1029/2020TC006431

Received 12 JUL 2020
Accepted 8 AUG 2021

Magmatism and Extension in the Anaconda Metamorphic Core Complex of Western Montana and Relation to Regional Tectonics

Caden J. Howlett[1,2], Aislin N. Reynolds[1], and Andrew K. Laskowski[1]

[1]Department of Earth Sciences, Montana State University, Bozeman, MT, USA, [2]Now at Department of Geosciences, University of Arizona, Tucson, AZ, USA

Abstract Metamorphic core complexes (MCCs) are a product of crustal extension, but their dynamics are still debated. Early research suggests that the formation of MCCs in the western United States was due to gravitational collapse of crust that had been thickened during Cordilleran orogenesis. However, the instability of overthickened crust alone cannot explain the diachronous formation of core complexes with a strong spatial dependency, as there was relatively uniform crustal thickness along strike of the Cordillera. For this reason, there is an interest in what role other lithospheric processes (such as subducted slab removal) play in the evolution of MCCs. We investigate the role of such processes by determining the temporal relation between magmatism and extension in the Anaconda MCC (AMCC) of western Montana. Geologic mapping, zircon U-Pb geochronology, and zircon (U-Th)/He thermochronology reveal that the initiation of extension in the AMCC in the Eocene (~53 Ma) began at least 3 Myr after the emplacement of voluminous Paleocene two-mica plutons. We interpret that the AMCC is an example of a core complex that was primed for extension by magmatic thermal weakening and suggest that foundering of the Farallon flat slab and the onset of the ignimbrite flareup in western Montana was responsible for the initiation of AMCC extension. An updated compilation of MCC cooling ages and Cenozoic volcanic activity across the western United States supports previous interpretations that the removal of Farallon oceanic lithosphere likely initiated MCC exhumation in some regions.

Plain Language Summary Horizontal extension of the Earth's crust can lead to topographic uplift and uncover rocks from depths of 10–30 km (the middle crust). The resulting geologic feature, consisting of ductilely deformed rocks underlying a low-angle normal fault, is known as a metamorphic core complex (MCC). MCCs are important because they record properties of crust that would otherwise be unreachable. Despite their importance, the mechanisms that cause core complexes to form are not well understood. In this study, we use field and radiometric dating techniques to determine the role that magmatism (intrusion of molten rock into the crust) served in the evolution of the Anaconda MCC in western Montana. We also compile data from the western United States, which suggest that the removal of a previously subducted tectonic plate from beneath North America caused some core complexes to form.

1. Introduction

Metamorphic core complexes (MCCs) are domal geological structures that result from the exhumation of the mid-to-lower crust (e.g., Crittenden et al., 1980). These structures are significant because they represent locations of extreme crustal extension and provide illuminating windows into the thermomechanical properties of Earth's lithosphere (e.g., Platt et al., 2015; Whitney et al., 2013). First described in the western United States, MCCs consist of a ductilely deformed metamorphic-plutonic footwall separated from a brittlely deformed hanging wall by a low-angle normal fault (detachment fault) (Armstrong, 1982; Coney, 1980; Wernicke, 1981). Despite their widespread occurrence and tectonic significance, the origin of core complexes—specifically the regional tectonic processes that facilitate footwall exhumation from mid-crustal depths—remains controversial (e.g., Konstantinou et al., 2013). Several orogen-scale dynamic models have been proposed for MCC formation in the North American Cordillera, including: (a) a change in plate motions, (b) dynamic processes of the downgoing slab (e.g., slab rollback), and (c) late or post-orogenic collapse due to overthickened continental crust (e.g., Whitney et al., 2013). In the North American Cordillera, MCCs form an N-S trending belt that traces a pre-extensional lithospheric welt, where crustal thicknesses

and gravitational potential energy would have been at their greatest prior to exhumation (Figure 1; Coney & Harms, 1984). This has led some researchers to conclude that core complex formation was primarily driven by post-orogenic gravitational collapse (e.g., Coney & Harms, 1984; Spencer & Reynolds, 1990; Wernicke et al., 1987). However, the instability of overthickened crust alone cannot explain the diachronous formation of core complexes (older in north, younger in south), as there was a relatively uniform crustal thickness along Cordilleran strike (Bahadori et al., 2018; Coney & Harms, 1984; Elison, 1991; Liu, 2001). For this reason, there is a growing interest surrounding the role that magmatic and sublithospheric processes played in the formation of core complexes (e.g., Cassel et al., 2018; Konstantinou et al., 2013; Stevens et al., 2016; Wernicke, 1992).

The spatial and temporal overlap of magmatic activity with MCC exhumation has led many researchers to consider the role of magmatism in the genesis of these structures (e.g., Armstrong & Ward, 1991; Foster et al., 2001; Lister & Baldwin, 1993; Wernicke, 1992). It is established that the presence of melt and resulting decrease in crustal strength and viscosity can trigger large-magnitude extension and core complex exhumation during the collapse of an orogenic system (e.g., Armstrong, 1982; Armstrong & Ward, 1991; Gans et al., 1989; Stevens et al., 2016; Vanderhaeghe & Teyssier, 2001). The process of partial melting and the release of volatiles during magmatism have been proposed as mechanisms for localizing strain and causing a rotation in the orientation of principle stresses, which in turn facilitates slip on low-angle normal faults (e.g., Parsons & Thompson, 1993). Numerous studies have documented that partially molten crust (which can result from magmatic addition to the lower crust) is weak and able to undergo flow (Kruckenberg et al., 2008; Whitney et al., 2004), which may also lead to MCC formation. Gans and Bohrson (1998) point out that in highly extended domains such as the Basin and Range, an "active rifting" model in which magmatism precedes extension appears to be common. This relationship contrasts with a "passive rifting" situation in which stretching and thinning of the lithosphere causes decompression melting in the asthenosphere (e.g., Sengör & Burke, 1978).

Studies of various core complexes in the North American Cordillera expose differences in the volume and timing of magmatism relative to the onset and duration of extension (Whitney et al., 2013). For example, main-phase plutonism and dike crystallization in the footwall of the Priest River and Clearwater core complexes occurred during exhumation (Gaschnig et al., 2011; Stevens et al., 2016), while plutonism and dike emplacement in the Bitterroot core complex of western Montana appear to largely predate the onset of extension (e.g., Foster et al., 2001). These temporal variations highlight three possibilities in the context of MCC formation that are worth evaluating with modern geochronological and thermochronological techniques. The first is that magmatism triggers extension, in which case it is expected that voluminous magmatism would shortly precede and perhaps partially overlap with the onset of extension (e.g., Hill et al., 1995). A second possibility is that footwall magmatism is triggered by extension, a scenario that would be supported by pluton and dike crystallization ages that post-date the onset of exhumation (e.g., Stevens et al., 2016). The third possibility is that magmatism is not clearly related spatially or temporally with extension (e.g., Spencer et al., 1995).

In this research, we determine the relation between magmatism and extension in the Anaconda MCC (AMCC) of western Montana, USA through geologic mapping, zircon U-Pb geochronology, zircon (U-Th)/He thermochronology, and Lu-Hf isotopic analysis. U-Pb zircon ages from major plutons in the AMCC footwall are compared to (U-Th)/He cooling ages interpreted to record the timing of exhumation. Hf-isotope signatures enable the determination of whether melts were derived from crustal or mantle sources, which in turn can give insight into the lithospheric and/or sublithospheric processes associated with pre- and synextensional magmatism. Located within the Idaho-Montana segment of the Cordilleran magmatic arc and fold-thrust belt, we propose that the AMCC is a representative example of a core complex whose development was primed by voluminous subduction-related magmatism and crustal thickening through retroarc thrust faulting. Our results suggest that Cretaceous-Paleocene shortening and magmatism generated sufficient crustal thickness in the Cordilleran hinterland for the orogen to become gravitationally unstable (e.g., Coney & Harms, 1984; Constenius et al., 2003), and that the onset and southward sweep of the ignimbrite flare-up initiated core complex formation. We integrate our findings into a generalized tectonic model that explains the relationship between pluton emplacement and exhumation in the AMCC footwall. Our results

10.1029/2020TC006431

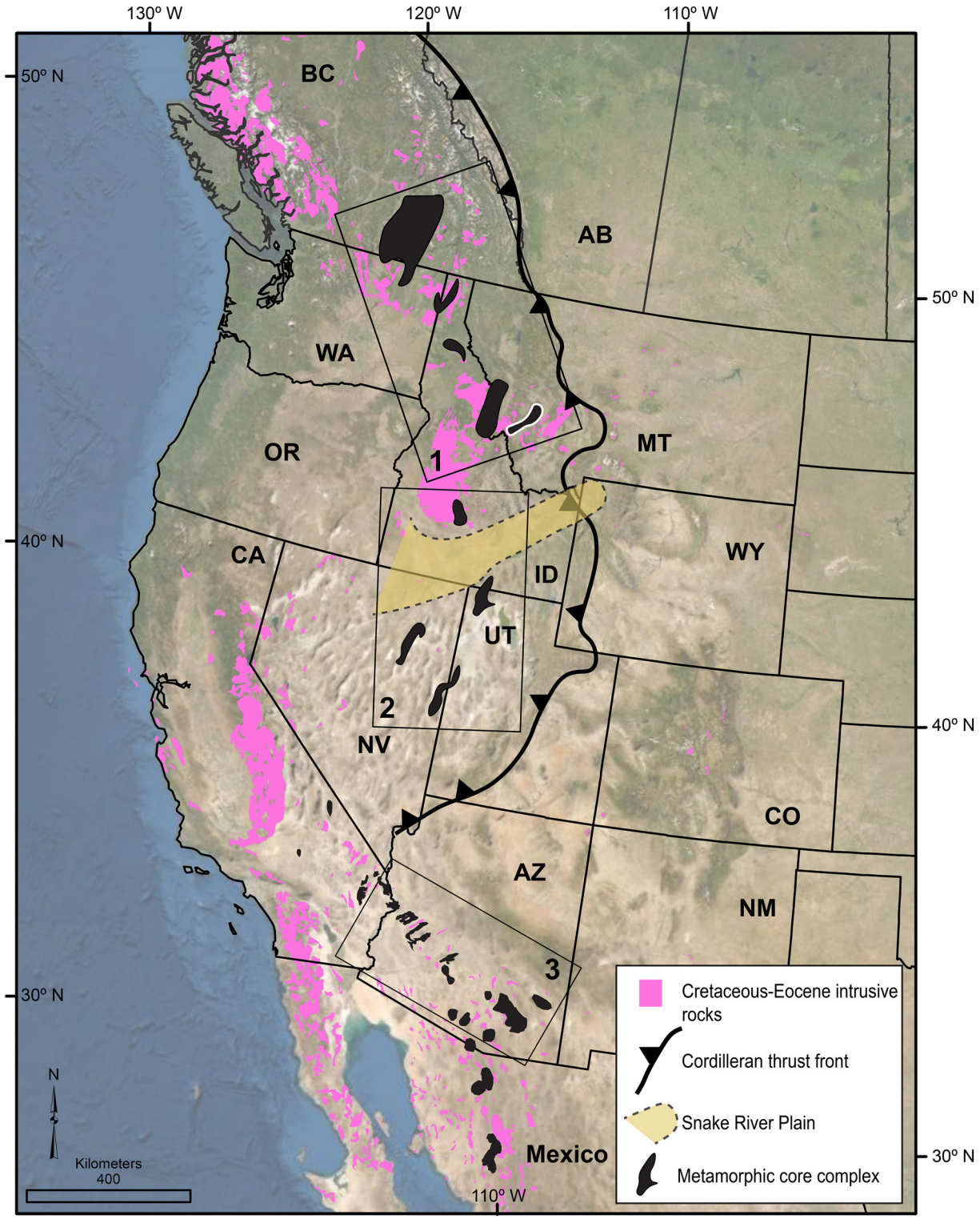

Figure 1. Tectonic overview map showing the distribution of major metamorphic core complexes and the aerial extent of Cretaceous-Cenozoic intrusive igneous rocks in the western United States (geology sourced from USGS National Map). MCC outlined in white represents Anaconda metamorphic core complex (AMCC). Black rectangles 1, 2, and 3 represent the northern, central, and southern MCC "belts" of the NA Cordillera, respectively. Basemap is satellite imagery from Esri/NOAA.

are compared with those from other core complexes, giving broader insight into the role that magmatic activity and sublithospheric processes may play in the collapse of a Cordilleran orogenic system.

2. Regional Geologic Setting

Cordilleran orogenic belts and accompanying magmatic arcs form as a response to the subduction of oceanic lithosphere beneath a continent (e.g., Coney & Reynolds, 1977; Dewey & Bird, 1970). The western United States developed into a Cordilleran-type margin with eastward subduction of the Farallon plate beneath North America in the Late Jurassic (e.g., DeCelles, 2004; Dickinson et al., 1996; Hamilton, 1969; Mulcahy et al., 2018). Over the following ~100 Myr, contractile deformation and magmatism migrated inboard over 1,000 km from the modern trench (Coney & Reynolds, 1977). Low-angle eastward subduction of the Farallon plate led to the development of a retroarc fold-thrust belt far from the trench, with arc magmatism and crustal thickening by shortening and magmatic addition well into Laurentia (Bird, 1988; Carrapa et al., 2019; DeCelles & Graham, 2015; Dewey & Bird, 1970).

North of the Snake River Plain in northeastern Idaho and western Montana, Late Cretaceous thrust faulting was accompanied by the voluminous magmatism of the Idaho and Boulder batholiths (e.g., Foster et al., 2001) (Figure 2). Core complex extension and extensional collapse by the reactivation of thrust ramps began immediately following the end of thrusting in this region at ~55 Ma (Constenius, 1996; Sears & Hendrix, 2004). These extension episodes were contemporaneous with widespread explosive volcanism of the Challis-Absaroka-Colville-Kamloops-Bitterroot-Lowland Creek loop (e.g., Feeley, 2003; Foster et al., 2010). This belt of calc-alkaline and alkaline volcanic rocks—stretching from the northwestern United States into central British Columbia—broadly overlaps in space and time with the exhumation of core complexes in the upper plate (Armstrong & Ward, 1991). Voluminous plutons that are present in the lower plates of all northern belt MCCs overlap temporally with these volcanics as well (e.g., Foster et al., 2010; Grice, 2006).

In the Basin and Range Province south of the Snake River Plain, the period following regional folding and thrust faulting (Late Jurassic-earliest Cenozoic; DeCelles, 2004; Yonkee & Weil, 2015) was dominated by the north to south sweep of the ignimbrite flareup (Best & Christiansen, 1991; Best et al., 2016; Lipman et al., 1971). Farther to the south, in northern Mexico and Arizona, analogous magmatism occurred but migrated from SE to NW rather than N–S. Both fronts of magmatism converged in southernmost Nevada at ~20 Ma (Christiansen et al., 1992; Humphreys, 1995). Like the region north of the Snake River Plain, widespread volcanism in both of these regions was accompanied by large magnitude extension and core complex formation (Armstrong & Ward, 1991; Coney & Reynolds, 1977).

3. The AMCC

The AMCC is one of the most recently discovered core complexes in the North American Cordillera (Foster et al., 2010; O'Neill et al., 2004), and it represents one of nine MCCs north of the Snake River Plain that exhumed mid- to lower-crustal rock beginning in the Eocene (e.g., Coney & Harms, 1984; Whitney et al., 2013). The AMCC is located within the Idaho-Montana segment of the Cordilleran magmatic arc, along the eastern edge of the Cordilleran hinterland (Foster et al., 2010; O'Neill et al., 2004) (Figure 2). The voluminous Late Cretaceous Boulder and Idaho batholiths are exposed to the east and west of the AMCC, respectively (e.g., Gaschnig et al., 2011; Lageson et al., 2001). These three major features of southwest Montana are situated within the western and central parts of the Helena Salient, a major eastward-convex salient that marks the easternmost position of the Sevier fold-thrust belt (DeCelles, 2004; Lageson et al., 2001).

The AMCC can be subdivided into three domains that are characteristic of a Cordilleran-style MCC: (a) a hanging wall consisting of Cenozoic syn- and post-extensional sedimentary units overlain by unconsolidated Quaternary glacial deposits, (b) a locally mylonitic metamorphic-plutonic and metasedimentary footwall, and (c) a low-angle detachment fault along the eastern edge of the Anaconda Range that separates the hanging wall and footwall (Foster et al., 2010; O'Neill et al., 2004; Wallace et al., 1992).

The AMCC hanging wall, exposed in the Deer Lodge Valley to the north and the Big Hole Valley to the south (Figure 2), consists of a series of fault-bound basins that contain Eocene-Quaternary clastic, volcaniclastic, and volcanic strata (Foster et al., 2010; Grice, 2006). In the Deer Lodge Valley, the stratigraphically lowest

10.1029/2020TC006431

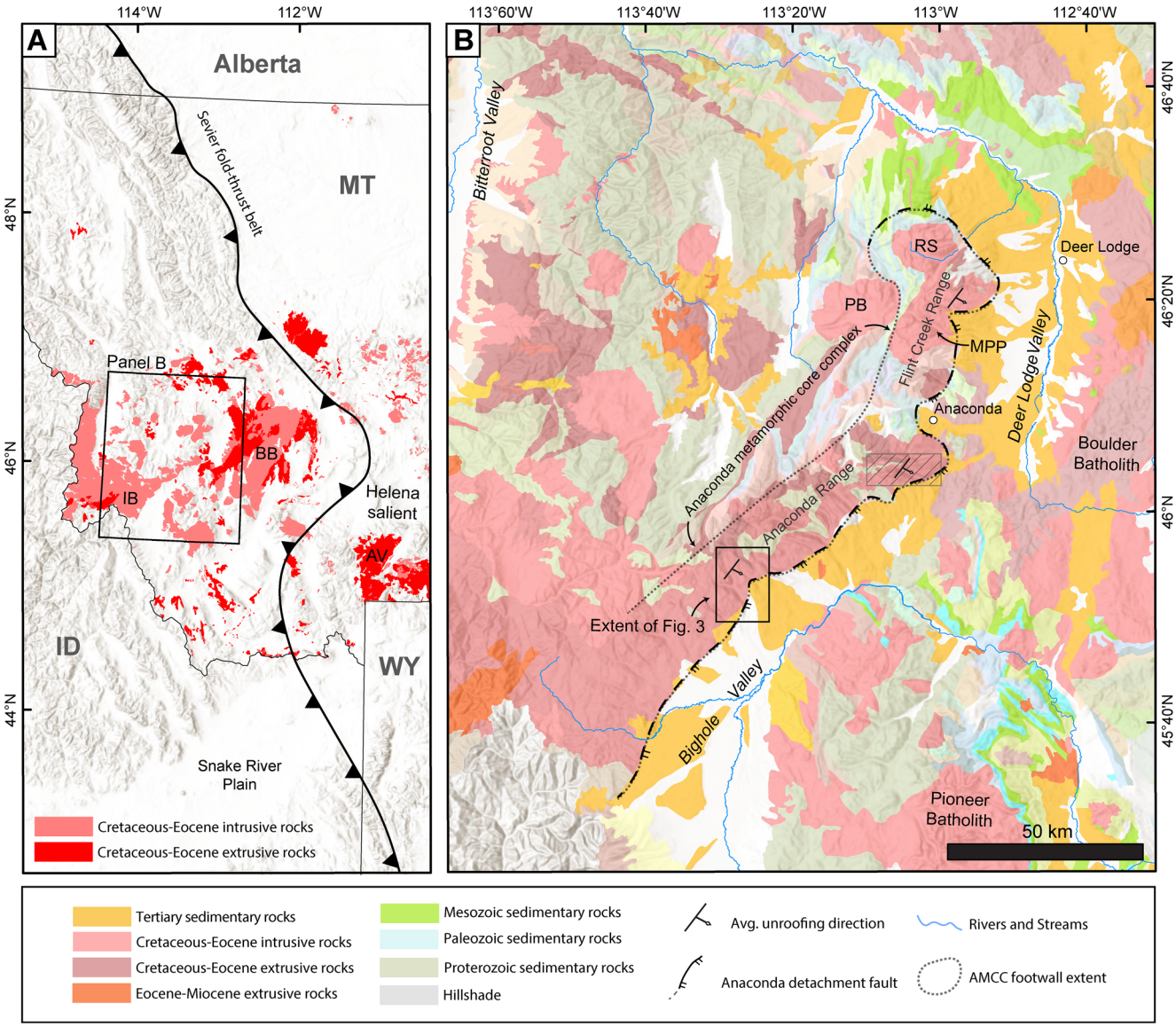

Figure 2. Tectonic overview maps showing (a) the Anaconda metamorphic core complex (AMCC) in the context of the western Montana segment of the North American Cordillera, displaying the distribution of Cretaceous-Cenozoic plutonic and volcanic rocks in relation to the Bitterroot MCC and the AMCC. AV, Absaroka Volcanics; BB, Boulder batholith; and IB, Idaho batholith. Map (b) displays a simplified geologic map of the AMCC, showing undivided Proterozoic-Cenozoic sedimentary and metasedimentary rocks and major plutons (legend below). Gray cross-hatched rectangle represents approximate location of Foster et al. (2010) transect location. The unroofing direction determined from the average trend of mineral stretching lineations and slickenlines is indicated for three regions along strike of the AMCC. MPP, Mount Powell Pluton; PB, Philipsburg batholith, and RS, Royal Stock. Bedrock geology data and hill shade basemap sourced from the Montana Bureau of Mining and Geology and Esri Online/NOAA, respectively.

units consist of poorly consolidated conglomerates, breccias, megabreccias, and sandstones that dip to the west-northwest at ~50–60° (Kalakay et al., 2003; O'Neill et al., 2004). These strata are overlain by more gently west-dipping (0–25°) lava flows, tuffs, and volcaniclastic units of the Lowland Creek Volcanics, which have produced $^{40}Ar/^{39}Ar$ cooling ages ranging from ~54 to 48 Ma (Dudás et al., 2010; Ispolatov, 1997; Kalakay et al., 2003). This timing constraint indicates that deposition in a supradetachment basin was occurring in the early to middle Eocene. In the Big Hole Valley, the Lowland Creek Volcanics are overlain by ashy sandstone and siltstone beds of the Eocene-Miocene Renova Formation. Zircons from an ash bed within the Renova Formation produced a U-Pb age of ~29.6 ± 0.01 Ma (Roe, 2010), and thin mafic flows interlayered with the top of the unit in the southern Big Hole Valley yielded a whole-rock K-Ar age of 21.9 ± 0.3 Ma (Fritz et al., 2007; Elliott, pers. comm). The poorly exposed Miocene Six Mile Creek Formation rests in

angular unconformity atop the Renova Formation in 7.5' quadrangles mapped in the south-central Big Hole Valley (Elliott, 2015, 2017; Figures 2 and 3). In both the Deer Lodge and the Big Hole Valleys, progressively less tilting of hanging wall strata moving up section suggest that they were deposited during and following movement along the Anaconda detachment fault (ADF) (Grice, 2006).

The footwall of the AMCC, extending from the Flint Creek Range in the north to the Anaconda Range in the south (Figure 2), is made up of Late Cretaceous to Eocene granitic plutons and dikes that intruded into the metamorphosed Mesoproterozoic Belt Supergroup and Middle Cambrian to Cretaceous strata (Desmarais, 1983; Emmons & Calkins, 1913; Foster et al., 2010; Grice, 2006; Lonn et al., 2003; Wallace et al., 1992). The Flint Creek Range is cored primarily by Late Cretaceous plutons, including the Mount Powell batholith and Royal Stock (O'Neill et al., 2004). The Anaconda Range footwall contains volumetrically smaller Late Cretaceous plutons and a large variety of early to middle Eocene dikes and plutons (Wallace et al., 1992). The central Anaconda Range is dominated by the Paleocene two-mica Pintler Creek Batholith (PCB), which has a weak SE-dipping protomylonitic foliation and hosts slip and stretching lineations with an average trend of ~138° (Figures 3a and 3b). Two-mica granites, as well as a variety of deformed and undeformed dikes, intrude predominately mixed metasedimentary rocks of a Belt Supergroup protolith (Wallace et al., 1992).

Separating the metamorphic-crystalline footwall from the Cenozoic sedimentary rocks of the hanging wall is the ~100 km long ADF. Along the Deer Lodge Valley, the ADF trends roughly N-S and dips gently (10–30°) to the east (Grice, 2006; O'Neill et al., 2004). From the Flint Creek Range to the northeastern Anaconda Range, the ADF is characterized by greenschist-facies mylonite, ultramylonite, and pseudotachylyte, and is overprinted by brittle normal faults (Foster et al., 2010). In the northeastern Anaconda Range, the ADF is expressed as a 300–500 m thick lower- to middle-greenschist-facies mylonitic shear zone (Foster et al., 2007, 2010). Exposures of the detachment become more isolated and lower-grade in the south-central and southern Anaconda Range (Elliott, 2017; Wallace et al., 1992; this study). In the south-central Anaconda Range, the detachment dips shallowly southeast (~12–15°), has been recognized as a complex zone of anastomosing brittle-plastic strain, and is expressed as multiple detachments in certain stretches along strike (Elliott, 2015; Howlett et al., 2020).

4. Methods

4.1. Igneous Zircon U-Pb Geochronology

Five intrusive igneous rocks were collected from bedrock exposures in the footwall of the AMCC for zircon U-Pb geochronology. Following collection, zircons were separated from bulk samples using standard density separation techniques at GeoSepServices in Moscow, ID. Separated zircons were mounted (~45 zircons/sample) alongside the SLmix, R33, and FC zircon standards in the sample preparation and mounting laboratory at Montana State University. Zircons were polished to a depth of ~30 μm and imaged using a scanning electron microscope with a cathodoluminescence (CL) attachment at Montana Tech CAMP Laboratory for targeting specific age domains during analysis. Backscattered electron (BSE) images of mounts, which serve as generalized maps for isotopic analysis, were obtained at the Imaging and Chemical Analysis Laboratory at Montana State University.

Zircon U-Pb ages were obtained for ~25 zircon grains per sample using a Photon Machines Analyte G2 Excimer laser attached to a Thermo Element2 HR single-collector ICP-MS at the University of Arizona Laserchron Center. Analysis and data reduction followed the detailed methods in Gehrels and Pecha (2014). Detailed sample locations given as GPS coordinates and raw data for U-Pb analysis for each sample are available in Table S1.

4.2. Igneous Zircon Lu-Hf Isotopic Analysis

Following the U-Pb isotopic analysis, Hf isotope measurements were made for select zircon grains from samples 061218CH1 ($n = 15$) and 071118CH5 ($n = 19$) using a Photon Machines Analyte G2 Excimer laser (40 μm beam diameter) attached to a Nu Plasma multicollector ICP-MS at the Arizona Laserchron Center. Measurements were made from the same sample spots as LA-ICPMS U-Pb analysis to ensure that

10.1029/2020TC006431

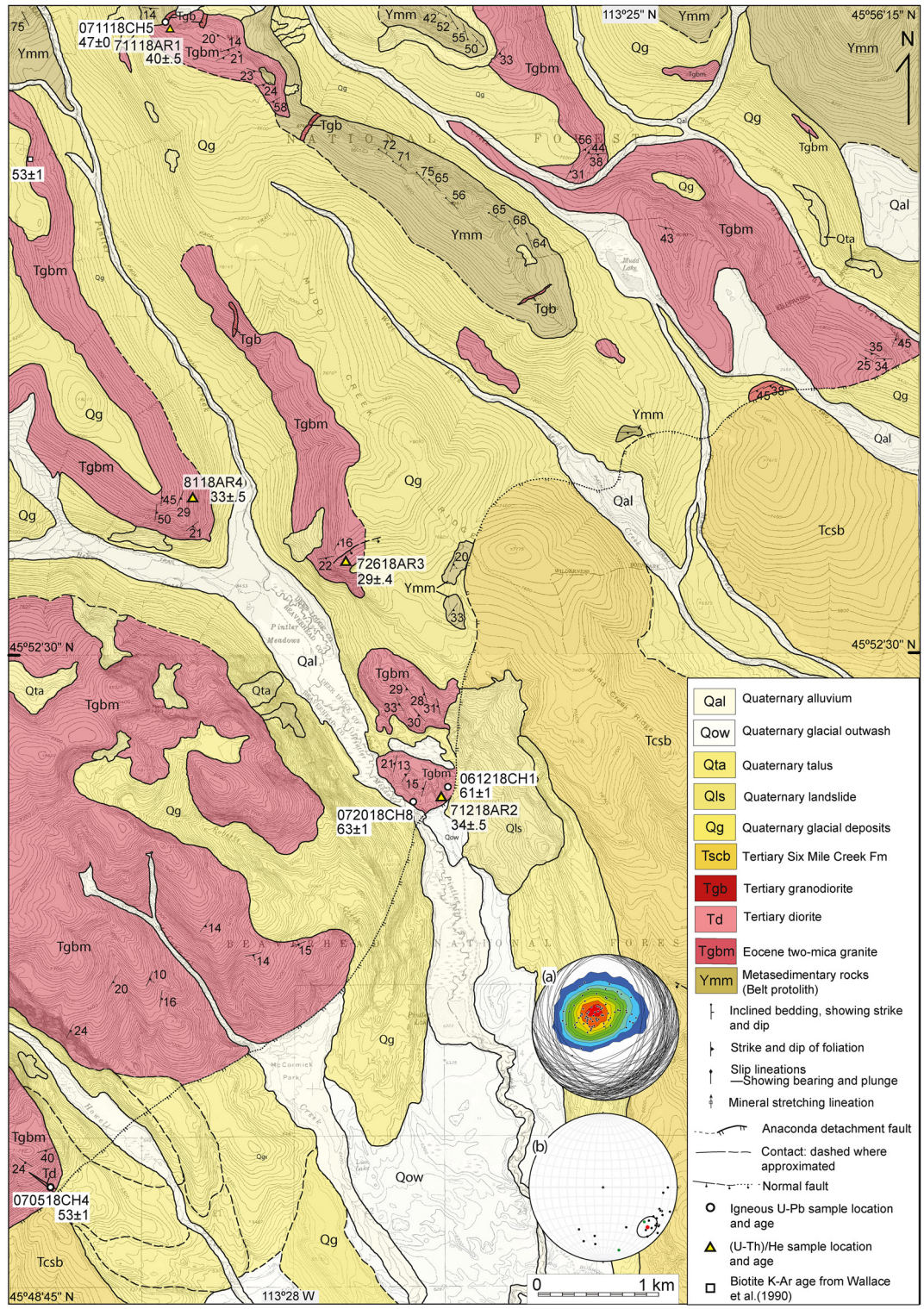

Figure 3. 1:24,000 scale geologic map of the field area in south-central Anaconda metamorphic core complex (AMCC). Overlapping structural measurements of similar orientation were averaged for clarity. Lambert equal area stereonets present. (a) Foliation planes and poles to foliation and (b) trend and plunge of slip and mineral stretching lineations (black and green, respectively) from the AMCC footwall. Average zircon (U-Th)/He and U-Pb ages and their associated uncertainties are displayed next to the sample location.

Hf isotopic data were determined from the same domain as the corresponding U-Pb age. Zircon fragments of MT, FC, SL, 91500, TEM, PLES, and R33 were used for standard sample bracketing during Lu-Hf analyses. All raw Hf isotope data are available in Table S2.

4.3. (U-Th)/He Thermochronology

Four samples of two-mica granite were collected from the footwall of the Anaconda detachment along a pseudo-vertical sample transect (Figure 3). Bulk samples were sent to GeoSepServices for mineral separation, and all four samples yielded sufficient quantities of zircon grains suitable for (U-Th)/He analyses. Conversely, samples yielded impure apatite separates dominated by small grains (<60 μm). Zircon grains were selected based on size, morphology, and clarity at the Montana State University Tectonic Sedimentology and Thermochronology Laboratory; euhedral grains of similar size with half widths >60 μm were selected and measured for α-ejection corrections (Farley et al., 1996). Twenty zircon grains were chosen for analysis and were individually packed into 1 mm Nb foil tubes to ensure even heating of the grain and prevent volitization of parent nuclides during Helium extraction. He extraction and measurement, as well as isotopic dissolution for U-Th-Sm content, were conducted following methods outlined in Reiners et al. (2004) at the University of Arizona Radiogenic Helium Dating Laboratory. Fish Canyon Tuff zircon standards of a known age were analyzed alongside unknowns to account for changes in isotopic fractionation or sensitivity bias. Analytical uncertainties, which are a combination of measurement and systematic error, commonly follow the order of 1%–3% at the 2-σ level (Reiners et al., 2004). Analytical errors reflect the propagation of uncertainty from measurements of ^{4}He, U, Th, and Sm and grain size. The reported error does not include error associated with the alpha ejection correction, which assumes a homogenous parent nuclide distribution within individual grains (Hourigan et al., 2005).

Inverse thermal modeling of low-temperature thermochronology data was completed using the HeFTy modeling software (Ketcham, 2005). HeFTy is based on a Monte-Carlo algorithm that accounts for both diffusive loss and radiogenic ingrowth of He for individual grains as a function of their thermal history, allowing the user to test a range of time-temperature (t-T) histories that could potentially provide good fits to the data.

5. Results

5.1. Geologic Mapping

We report field data collected from the south-central AMCC, ~30 km north of the town of Wisdom, Montana, USA. Field work was conducted in all three structural domains of the AMCC (hanging wall, footwall, and along the ADF). Mapping was conducted at ~1:24,000 scale across the study area (Figure 3) atop paper 7.5' topographic basemaps generated by the United States Geological Survey.

Unlike many core complexes in the North American Cordillera, the south-central AMCC footwall does not contain abundant mylonitic rocks or rocks that have undergone extensive migmatization. That said, the best exposures of protomylonitic rocks in the footwall are in the central field area (adjacent to geochronology samples 061218CH1 and 072018CH8; Figure 3). This approximately one square kilometer region is host to anastomosing zones of high shear, two-mica granite, granitic gneiss, and rare leucogranite dikes containing almandine garnet (Figures 4a–4c). Zones of high shear are interpreted to represent strands of the ADF, which is the dominant NE-SW trending structure in the map area (Figure 3). Field analysis of the very limited exposures of the ADF reveals protomylonites that extend no more than 100 m from the fault. Approximately 4 km to the northwest of the central map area, the zones of protomylonite disappear entirely and the ADF is characterized by prominent zones of cataclasite and chloritic breccias (Figure 4d). Similar cataclasites define the ADF in the Big Hole Battlefield Quadrangle ~20 km southwest of our map area (Elliott, pers. comm). These observations from the south-central and southern Anaconda Range differ from those in the northeastern Anaconda Range and Flint Creek Range, where the ADF is characterized by a relatively well-exposed, lower- to middle-greenschist-facies mylonite zone that is 300–500 m thick (e.g., Foster et al., 2010; O'Neill et al., 2004). The apparent decrease in metamorphic grade and amount of exposure along strike of the ADF could be explained by differences in the timing and/or magnitude of exhumation in each region, but additional work is required to address this observation.

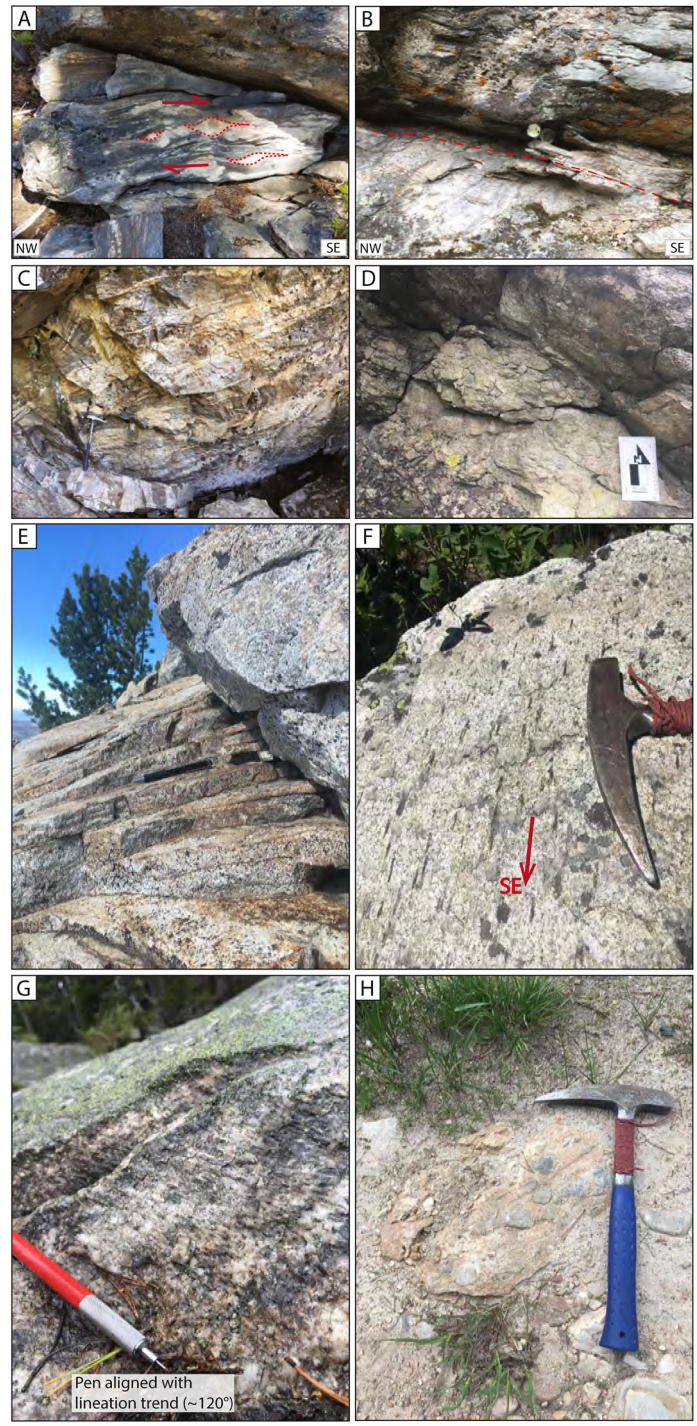

Figure 4. Field photographs from the south-central Anaconda metamorphic core complex (AMCC). (a) Protomylonite near Anaconda detachment in the central field area with top-to-southeast kinematics (red arrows). (b) One of several zones of high strain in the central field area dipping gently (~10°) to the southeast. Protomylonitic foliation traced as dashed red line. Brunton for scale. (c) Outcrop exposing the highest grade metamorphic rocks (granitic gneiss) in central field area; rock hammer for scale. (d) Zone of the Anaconda detachment in northeast field area characterized by zones of cataclasite and chloritic breccias. (e) Exfoliation of two-mica granite (Pintler Creek Batholith) occurring along SE-dipping foliation (defined by mica with subparallel alignment). Pen for scale. (f) NW-SE trending mineral stretching lineations in two-mica granite. Dark minerals are smeared biotite. (g) Elongate quartz in two-mica granite trending to the southeast. (h) A rare exposure of the Miocene Six Mile Creek Formation in the hanging wall of AMCC.

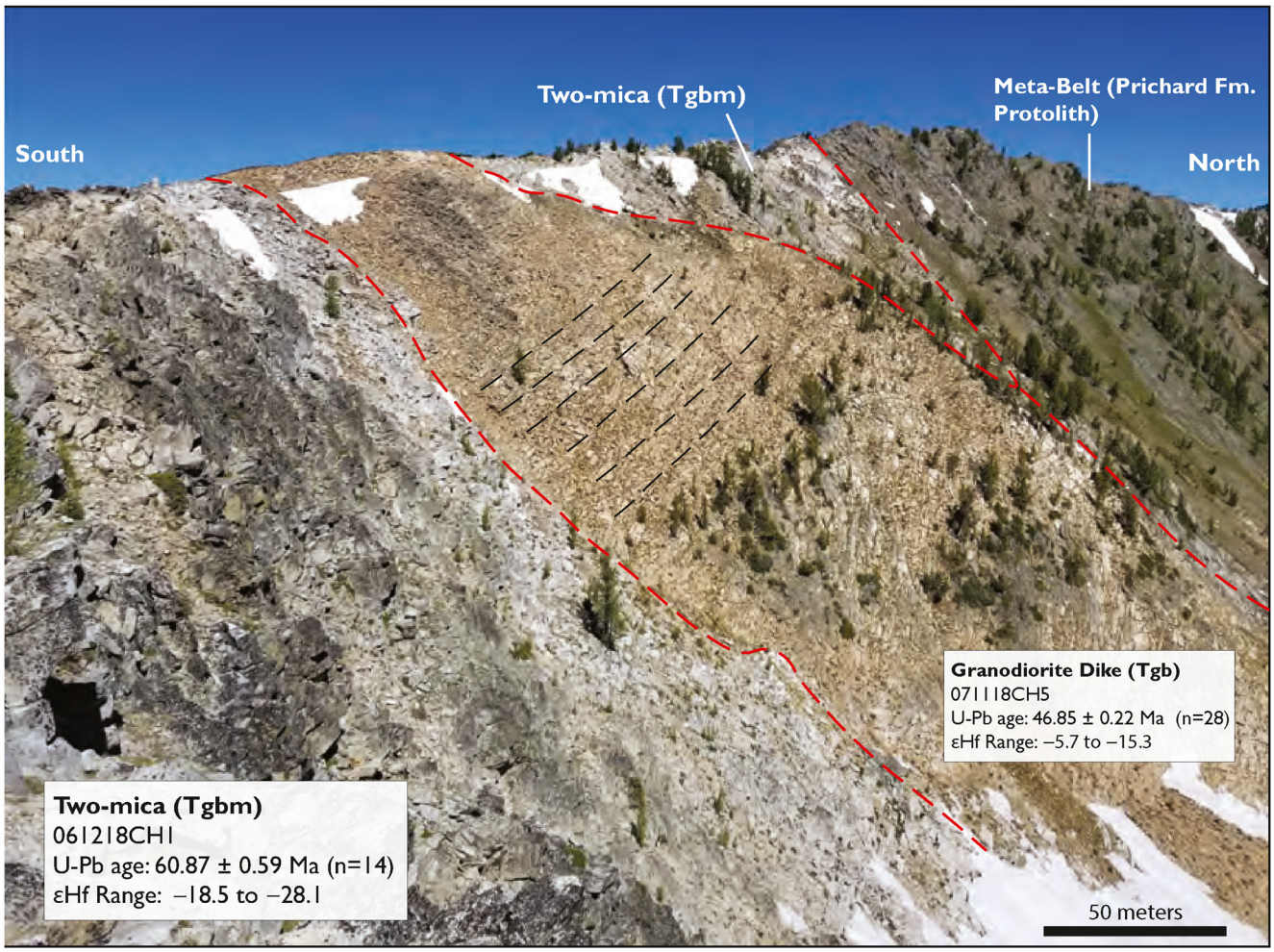

Figure 5. Anaconda metamorphic core complex footwall exposing ~47 Ma granodiorite dike intruding between ~61 Ma two-mica granite and metasedimentary Belt rock. Dashed red lines are rock unit contacts and dashed black lines trace south-dipping foliation. A similarly oriented foliation is recorded in the two-mica granite but is difficult to distinguish in this image due to a change in the ridge orientation. The representative U-Pb ages and ranges of εHf values are included for each sample.

The two-mica granite of the PCB dominates the footwall in the map area (Figures 3 and 5). The batholith intrudes into deformed metasedimentary rocks of the Belt Supergroup and has a weak south-southeast dipping foliation (Figures 3a, 4e and 5). Foliation within the PCB is of primarily sub-solidus tectonic origin and foliation planes are defined by muscovite and biotite with subparallel alignment. In the central field area, the foliation is more pronounced and is best described as protomylonitic, with minor grain-size reduction and occasional exposures of asymmetric porphyoclasts. Paterson et al. (1989) state that the most unambiguous field evidence for tectonic foliation in plutonic rocks is a foliation behavior that is independent of pluton boundaries. The remarkably consistent strike and dip of foliation in the PCB suggests that there is no dependence on proximity to pluton boundaries. Furthermore, tectonic foliation in plutonic rocks commonly has the same orientation as that in the host/wall rock, and the Belt Supergroup locally contains an S-SE dipping foliation near the Anaconda detachment (Figure 3). It is noteworthy that the present exposures of the PCB are probably near the original roof of the pluton, an interpretation that is supported by the presence of numerous roof pendants in the south-central Anaconda Range (Wallace et al., 1992). In the northern map area, the northeast-dipping metasedimentary Belt Supergroup rocks likely represent one of these pendants (Figure 3).

Mineral stretching lineations are present in the PCB, trend east-southeast, and are defined by elongate quartz and smeared mica (Figures 4f and 4g). Ridge-in-groove-type striations (ductile or "hot" slickensides) and

brittle slip lineations are also abundant and occur along foliation planes with the same trend as stretching lineations. Hot slickensides expose striations along the C-surface of foliation and usually display a "shiny" surface similar to normal slickenlines, allowing them to be distinguished from stretching lineations (e.g., Lin et al., 2007). Although their occurrence is rare, sigma clasts are present within and directly adjacent to the ADF which show top-to-the-southeast shear (Figure 4a). Kinematics of tightly folded leucocratic bands within gneiss in the central field area suggest the same kinematics (top-to-SE). The trend and plunge of mineral stretching lineations, hot slickensides, and slip lineations, combined with asymmetric shear sense indicators, suggest unroofing was directed to the southeast, with an average trend and plunge of 138°, 19 (Figures 3b, 4f and 4g). These data agree with previous measurements in the AMCC footwall that indicate east-southeast directed unroofing based on slip and stretching lineations, asymmetric porphroclasts, and mica fish (e.g., Elliott, 2015; Foster et al., 2010; O'Neill et al., 2004).

The PCB is crosscut by variably deformed granodiorite and dacite dikes (e.g., Wallace et al., 1992; this study). An Eocene granodiorite dike near the northern extent of the map area exploits a discordant contact between the PCB and mixed metasedimentary Belt rocks (Figure 5). This dike exhibits a well-developed foliation that has a strike and dip similar to that observed in the PCB. In contrast, an Eocene dacite dike in the southern map area displays no foliation and no other evidence of deformation.

Poor exposure of the hanging wall of the AMCC in our map area limits interpretation. The Miocene Six Mile Creek Formation is the only Cenozoic hanging wall unit identified in the map area, consisting primarily of moderately sorted, well-rounded, gravel-sized quartzite clasts (Figure 4h). The matrix consists of moderately sorted, red- and tan-colored sand particles that range from medium- to coarse-grained (Figure 4h). Both the Six Mile Creek Formation and the ADF are usually concealed beneath Quaternary glacial and alluvial deposits. In places where the ADF is covered by Quaternary sediments, there is usually an abrupt change from unconsolidated well-rounded quartzite and granitic cobbles characteristic of the Six Mile Creek Formation to the low-grade metamorphic (greenschist facies) and foliated rocks of the AMCC footwall. This abrupt change in float occurring along the ADF has been observed along strike (e.g., Elliott, 2015), and it is possible that it represents an area where the main detachment is cutting the Six Mile Creek Formation. While it is possible that faulting ceased before Miocene deposition and that sediments are draped across the faults, the coincidence between the topographic lineament and an abrupt change in surface float argues against it (Elliott, pers. comm). No valuable bedding measurements were obtained from the Six Mile Creek Formation due to poor exposure and lack of consolidation. If future studies find Miocene strata to be dipping toward the ADF, it will offer additional support for the interpretation that the detachment may have crosscut and rotated these younger units. Previous workers concluded that extension on the detachment ended in Oligocene times, and Foster et al. (2010) used a variety of thermochronology data to establish movement from ~53 to 27 Ma. If the ADF truly offsets the Six Mile Creek Formation, movement along the detachment must have occurred more recently.

5.2. Zircon U-Pb Geochronology and Lu-Hf Isotopic Results

5.2.1. Sample 071118CH5

Sample 071118CH5 was sampled from a granodiorite dike with discordant contacts between Mesoproterozoic metasedimentary rock and two-mica granite near the northwest corner of the map area (Figures 3 and 5). The sample is a fine- to medium-grained granodiorite consisting of plagioclase, quartz, biotite, potassium feldspar, and minor hornblende (Figure 6a). Quartz phenocrysts commonly are rounded. Zircons display simple igneous growth zoning and U-Pb dates range from 45.7 ± 0.7 to 48.8 ± 0.8 Ma ($n = 31$). The weighted-mean age of 28 grains is 46.85 ± 0.22 Ma (MSWD = 4.4) (Table 1 and Figure 7). εHf values vary from −5.7 to −15.3 at 47 Ma ($n = 19$) (Figure 8).

5.2.2. Sample 071918CH7

Sample 071918CH7 was obtained from ~130 m north of the northern extent of the mapped area (Figure 3). It is a dacite dike consisting of plagioclase, biotite, clinopyroxene, quartz, and minor hornblende (Figure 6b). Zircon grains display simple igneous growth zoning, with dates ranging from 50.2 ± 0.4 to 54.5 ± 0.8 Ma ($n = 29$). The weighted-mean age of 25 grains is 51.04 ± 0.25 Ma (MSWD = 4.0) (Figure 7).

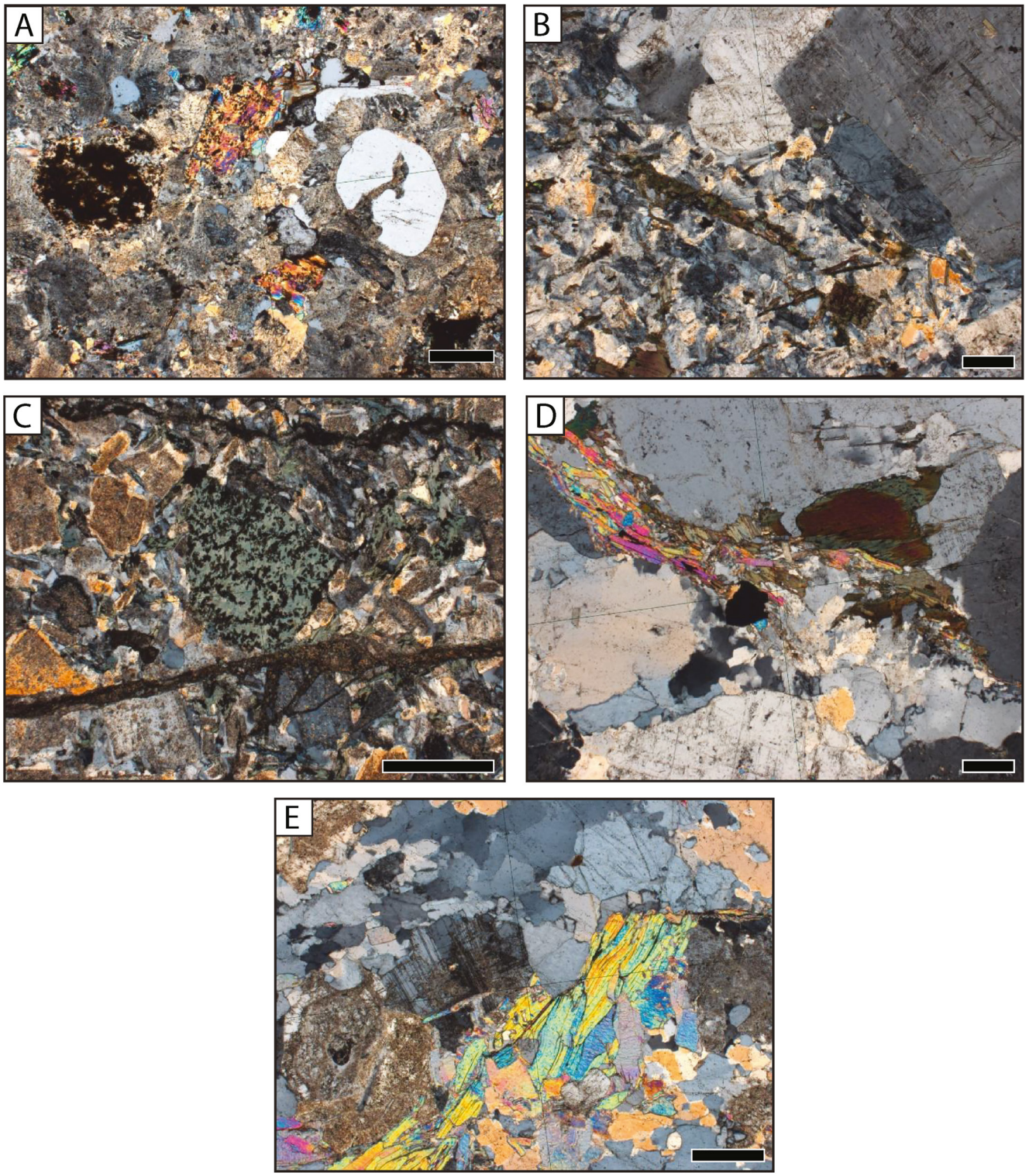

Figure 6. Representative thin section photomicrographs for each U-Pb geochronology sample. (a–e) show samples 071118CH5, 071918CH7, 070518CH4, 061218CH1, and 072018CH8, respectively. Scale bars are 2 mm.

Table 1
Summary Table for Igneous Zircon U-Pb Samples

Sample	Latitude (°N)	Longitude (°W)	Type of analysis	Weighted mean $^{238}U/^{206}Pb$ age (Ma)	Error (Ma)[a]	MSWD[b]	Comments
061218CH1	45.862	113.440	LA-ICPMS	60.87	0.59	6.8	061218CH1 and 072018CH8 are from two-mica granites and produce complex U-Pb ages with multiple age domains. The weighted mean ages reported here represent the dominant population in each sample. See Text S1 and Table S1 for more information.
072018CH8	45.861	113.446	LA-ICPMS	62.70	1.5	3.2	
070518CH4	45.824	113.495	LA-ICPMS	52.75	0.61	7.8	Undeformed dacite dike in southern field area.
071118CH5	45.936	113.480	LA-ICPMS	46.85	0.22	4.4	Granodiorite dike in northern field area. See Figure 5 for dike field relationship.
071918CH7	43.939	113.438	LA-ICPMS	51.04	0.25	4	Sampled ~130 m north of map area.

Note. See Figure 7 for U-Pb weighted mean plots.
[a]2σ errors. [b]Mean square weighted deviation.

5.2.3. Sample 070518CH4

Sample 070518CH4 was obtained from an undeformed dacite dike that crosscuts the two-mica granite in the southwestern map area, near the Anaconda detachment (Figure 3). Dominant minerals present include plagioclase, quartz, biotite, potassium feldspar, and rare hornblende (Figure 6c). Phenocrysts of potassium feldspar are commonly rimmed by plagioclase. The sample contains large (>1 cm) plagioclase phenocrysts and is undeformed with no magmatic or tectonic foliation (Figure 6c). Veinlets interpreted to be associated with hydrothermal alteration are present (Figure 6c). The zircon yield from this sample was relatively low and small zircon size (50–60 μm) made any zircon zoning indiscernible. Zircon analyses provide U-Pb dates that vary from 51.4 ± 0.9 to 56.3 ± 1.1 Ma (n = 15). The weighted-mean age from 14 grains is 52.75 ± 0.61 Ma (MSWD = 7.8) (Figure 7).

5.2.4. Sample 061218CH1

Sample 061218CH1 is a fine- to medium-grained two-mica granite that is generally porphyritic. Major minerals include plagioclase, quartz, potassium feldspar, green and brown biotite, and muscovite (Figure 6d). Quartz exhibits rare undulose extinction, potassium feldspar is commonly fractured and shows wavy extinction, and biotite is partly altered to chlorite and secondary muscovite. Mica in the sample exhibits subparallel alignment, which in outcrop usually defines the south-southeast dipping foliation. Trace amounts of accessory zircon, apatite, epidote, and opaque minerals are also present. BSE and CL imaging expose that many zircons display oscillatory zoning, with some zoning around distinct cores, suggesting igneous growth around inherited cores. The 19 youngest zircon U-Pb ages for sample 061218CH1 range from 59.3 ± 0.8 to ~74.5 Ma, and ages for six cores range from 1662.5 ± 11.1 to 1799.2 ± 17.5 Ma. This wide range of young ages makes it difficult to obtain a reliable mean U-Pb age; thus, we separated the ages into dominant populations in an attempt to isolate the youngest dominant populations. The weighted-mean age for the selected young population is 60.87 ± 0.59 Ma (n = 14, MSWD = 6.8) (Figure 7). εHf values from igneous rims vary from −28.1 calculated at 61 Ma to −18.5 at 62 Ma (n = 15) (Figure 8).

5.2.5. Sample 072018CH8

Sample 072018CH8 is a porphyritic two-mica granite that has the same mineral composition as 061218CH1. Collected close to one of the major shear zones in the central map area, the quartz in this sample exhibits more intense undulose extinction than in 061218CH1, suggestive of a greater amount of internal strain (Figure 6e). Aligned and subtly folded micas offer additional support for internal strain. Zircons extracted

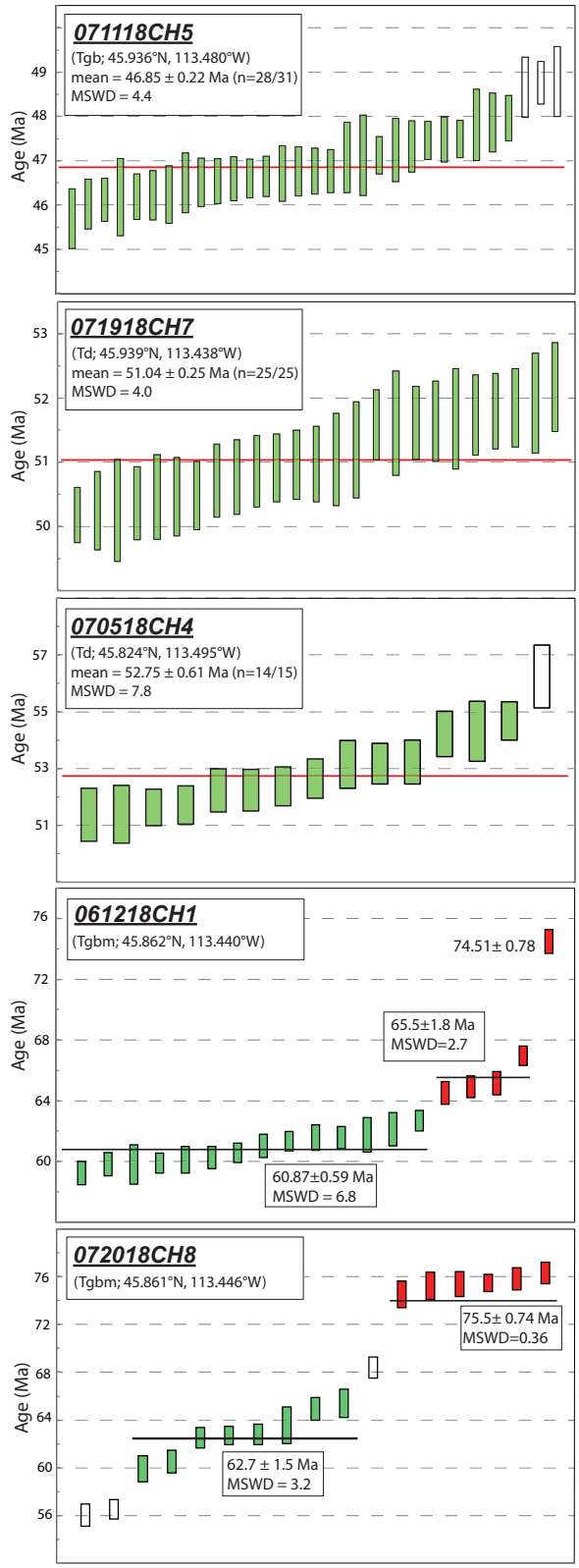

Figure 7. Igneous zircon U-Pb geochronology weighted mean plots from representative igneous rocks exposed in the Anaconda metamorphic core complex (AMCC) footwall. Plots for the two-mica granite of the Pintler Creek Batholith (061218CH1 and 072018CH8) expose the complexities of youngest rim ages. Cretaceous age grains in both are interpreted to have been incorporated into two-mica melt from existing plutons in AMCC footwall. Hollow boxes are considered outliers and are not included in MSWD calculation. Sample locations are labeled on geologic map in Figure 3.

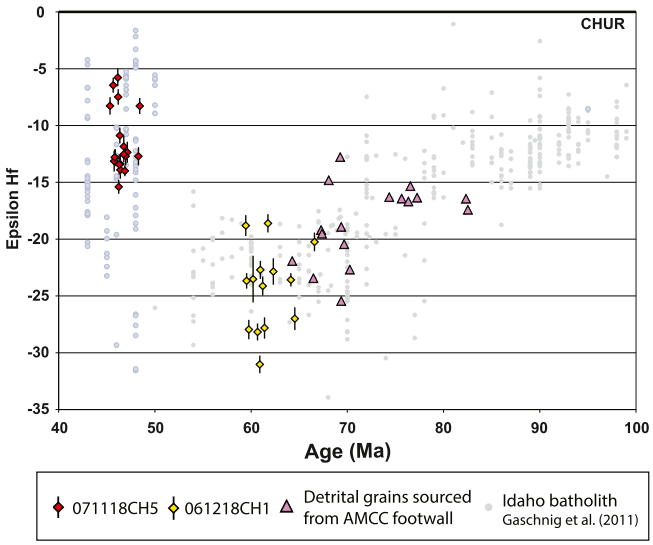

Figure 8. εHf values versus U-Pb age for the synextensional granodiorite dike (071118CH5), the two-mica granite (061218CH1), and Cretaceous detrital zircons extracted from Anaconda metamorphic core complex (AMCC) supradetachment basin (Howlett & Laskowski, 2021). Results from AMCC plotted atop εHf evolution of the Idaho Batholith (gray circles), located ~100 km to the west of our field area (Gaschnig et al., 2011). See text for discussion. Bold black line represents chondritic uniform reservoir (CHUR).

from the sample display oscillatory zoning, with some zoning around inherited cores. The 17 youngest zircon ages range from 56.1 ± 0.9 to 76.3 ± 0.9 Ma, and ages for nine cores range from 1475.4 ± 17.7 to 2755.0 ± 10.9 Ma. The weighted mean age of the eight grains selected as the dominant age population is 62.7 ± 1.5 Ma (MSWD = 3.2) (Figure 7). The higher-than-optimal MSWD values in both our two-mica samples might reflect longer-duration zircon crystallization than analytical precision or mixing between crystallization age rims and xenocrystic cores during ablation. CL images with spot locations and corresponding ages for individual grains are available in Figure S1.

5.3. Zircon (U-Th)/He Results

Eighteen zircon grains from four two-mica granite samples produced useful (U-Th)/He cooling ages (Table 2; detailed data available in Table S3). A wide spread of cooling ages is recorded for each sample, with individual zircon He ages ranging from 41.4 ± 0.6 Ma to 8.7 ± 0.1 Ma (Figure 9; Table S3). Most grains yielded ages between 38 and 28 Ma (Figure 9). Ages from sample 71118AR1 range from 31.6 ± 0.4 to 41.4 ± 0.6 Ma and ages from sample 71218AR2 range from 8.7 ± 0.1 Ma to 35.5 ± 0.5. Samples 72618AR3 and 8118AR4 yielded cooling ages from 24.7 ± 0.3 to 29.7 ± 0.4 and 28.2 ± 0.4 to 38.4 ± 0.5, respectively (Figure 9). The single age of 8.7 ± 0.1 Ma in sample 71218AR2 was a significant outlier (the next-youngest age is 24.7 ± 0.3 Ma), and was not used in calculations or model inputs due to potential for analytical errors or damage/loss of helium from the grain prior to analysis.

The highest elevation sample yielded the oldest cooling age (Figure 9a), consistent with passage through the zircon He partial retention zone (PRZ) earliest during exhumation. However, the lowest elevation sample did not yield the youngest cooling age as expected. Variability of zircon He ages in a given sample may indicate their presence in the PRZ (140–200°C) between 38 and 28 Ma. If samples had cooled through the PRZ very rapidly, they would likely record a narrower range of cooling ages. Four plots were constructed to investigate why the second-highest elevation sample (72618AR3) yielded the youngest cooling ages rather than the lowest elevation sample (Figure 9). Correlation between sample age and effective uranium (eU = 0.235Th × U) was explored as a possible explanation, with eU acting as a proxy for radiation damage that could affect closure temperatures of individual grains (Flowers et al., 2009; Guenthner et al., 2013). Figure 9b shows slightly positive age-eU correlations, but the youngest grains do not correlate with the highest eU (two grains > 1,700 ppm); thus eU does not appear to represent a significant control. Furthermore, U-Pb crystallization ages of nearby samples are <80 Ma, limiting the time in which radiation damage could accumulate. Ages also show no correlation to grain size (Figure 9c); the oldest sample (71118AR1) contains a cluster of three ages at ~40 Ma, regardless of variations in spherical radii (Rs) between ~37 and

Table 2
Summary Table for Igneous Zircon (U-Th)/He Samples

Sample	Latitude	Longitude	Elevation (m)	Distance from detachment (km)[a]	Mean ZHe age (Ma)	2σ error (Ma)	n[b]
71118AR1	45.936	113.48	2,823	6.38	39.81	0.51	(5/5)
71218AR2	45.862	113.44	1,973	0.165	34.44	0.47	(4/5)
72618AR3	45.884	113.456	2,367	1.96	29.26	0.39	(4/5)
8118AR4	45.888	113.474	2,112	4.5	33.16	0.46	(5/5)

Note. See Table S3 for details.
[a]Represents distance from sample location to detachment; azimuth equal to approximate unroofing direction. [b]Four fifths indicates four out of five grains analyzed were used to calculate mean ages.

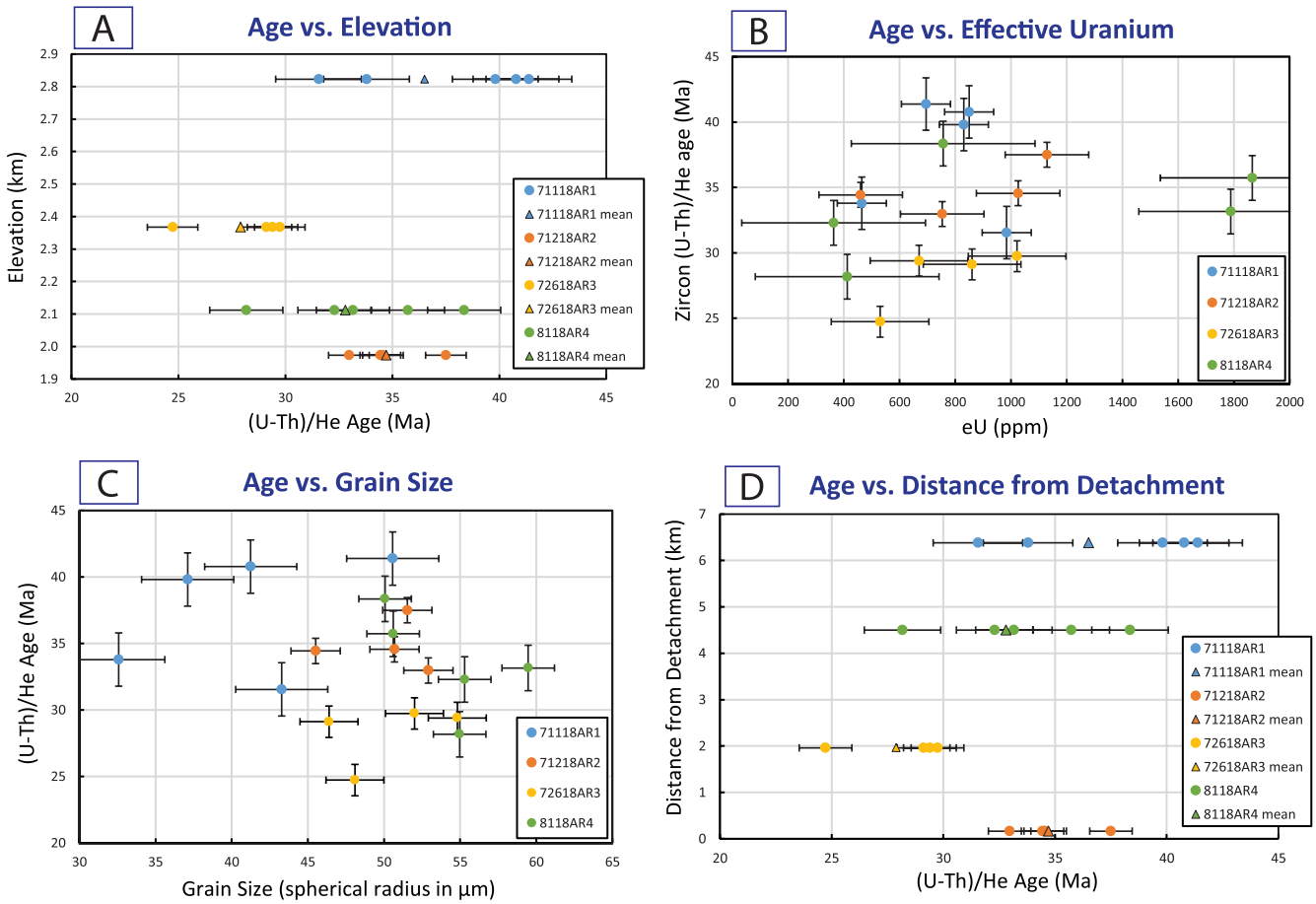

Figure 9. (a) Elevation versus zircon (U-Th)/He age, triangles are weighted means for each sample. (b) Zircon (U-Th)/He ages as a function of effective uranium (eU = 0.235Th × U). Slightly positive age-eU correlations are not interpreted to be strong enough evidence to cause the observed irregularity in ages. (c) Age versus grain size, showing no strong correlation. (d) Age as a function of sample distance from the Anaconda detachment; measured as a straight-line from sample to mapped fault with azimuth equal to approximate unroofing direction. Sample ages show a clear trend of increasing cooling age with distance from the detachment, apart from the irregular sample nearest to the detachment, which may indicate movement and exhumation along an older structure within the detachment zone.

50 µm. Figure 9d plots cooling age as a function of sample distance from the Anaconda detachment in order to examine potential structural controls. Straight-line measurements were made from each sample to the detachment with an azimuth approximating that of the unroofing direction. In places where the detachment was concealed, a DEM was used to identify its topographic expression. The samples show a clear trend of increasing cooling age with distance from the detachment, apart from the sample collected from the lowest elevation and very near to the detachment, which yielded older ages than the two samples from higher elevations.

5.3.1. HeFTy Thermal Modeling Inputs and Results

Inverse modeling of 50,000 paths for each sample was completed against t-T constraints defined by the zircon (U-Th)/He ages and zircon U-Pb crystallization ages from this study and previously published apatite fission track and muscovite and biotite $^{40}Ar/^{39}Ar$ ages (Figure 2; Foster et al., 2010). Closure temperatures for these systems can vary due to factors such as cooling rate, grain size, radiation damage, crystal chemistry, and zonation, but approximate closure temperatures are 450–350°C for muscovite $^{40}Ar/^{39}Ar$ and 380–310°C for biotite $^{40}Ar/^{39}Ar$ (e.g., McDougall & Harrison, 1999), 190–170°C for zircon (U-Th)/He (e.g., Guenthner et al., 2013), and 110–60°C for apatite fission track (e.g., Green et al., 1986). Age inputs for each model were a representative grain with a median age from each sample and the corresponding error, radius, and concentrations of U and Th measured for each of the four representative grains. The searchable t-T

space for thermal history paths was defined by the following five input parameters, represented graphically in model runs as boxes through which the modeled t-T paths were forced:

1. Zircon U-Pb crystallization ages from two-mica granitic plutons from this study indicate that the sample was at temperatures >900°C until between 65 and 60 Ma.
2. Muscovite (450–350°C) and biotite (380–330°C) from granites recorded $^{40}Ar/^{39}Ar$ cooling ages between 53 and 39 Ma, indicating that samples must have experienced rapid cooling through these temperatures by early to middle Eocene time (Foster et al., 2010).
3. Zircon (U-Th)/He ages from this study indicate that samples cooled between 190 and 170°C from 42 to 25 Ma. These constraints were enforced within the He model for each sample rather than as a t-T box.
4. Apatite fission track ages were less well constrained, indicating cooling through 110–60°C between 40 and 20 Ma (Foster et al., 2010).
5. Samples were collected at the surface (20–0°C) at 0 Ma.

The t-T paths resolved by the HeFTy thermal model for each sample are shown in Figure 10 as a series of good fit (blue) and acceptable fit (green) path envelopes, along with the single best fit path (black) and weighted mean of good fit paths (blue). The first model that was run for each sample was minimally restricted, with the only constraints being zircon U-Pb crystallization age, zircon (U-Th)/He data from the sample, and sample collection at the surface, allowing HeFTy to more freely produce thermal histories. The second model for each sample was restricted by all of the five constraints listed above, allowing for a comparison of this study with results from Foster et al. (2010).

Under the less constrained model parameters, HeFTy produced a wide range of potential t-T paths, but all four samples generally show rapid cooling from ~60 to ~30 Ma (Figure 10). The best fit line for sample 71218AR2 is comparatively an outlier, showing a plateau at 900° from 60 to ~48 Ma, followed by extremely rapid cooling from ~48 to ~34 Ma. The more constrained models show similarly rapid cooling between 60 and ~30 Ma for the weighted mean of each sample, followed by an ~8 Myr reduction in the cooling rate. The best fit line for sample 71218AR2 once again shows a plateau, though less pronounced, from 60 to ~55 Ma, followed by a steeper slope until ~30 Ma, at which point cooling slows dramatically. A similar, more pronounced plateau and subsequent rapid cooling trend is seen in the best fit line for the generated t-T paths for sample 71118AR1. The paths for all four samples show a flattening of slope between ~45 and 25 Ma. Based on the thermochronology data and weighted mean t-T paths generated in HeFTy, results favor initially rapid cooling (~33°/m.y) from >900°C at ~60 Ma to 450–300°C by ~45 Ma, followed by a second episode of slower cooling at a rate of ~16°/m.y. from ~45 to ~25 Ma (Figure 10). The fact that all models generate similar t-T paths is an indication that the imposed constraints from Foster et al. (2010) provide a good fit to our data and do not overinfluence the models. This further implies that their study area (~50 km to the NE in the footwall of the Anaconda detachment) likely experienced a similar thermal history to that reported in this study.

6. Discussion

6.1. Footwall Magmatism and Cooling History

U-Pb zircon geochronology on variably deformed igneous rocks (ranging in composition from granodiorite to dacite) in the AMCC footwall provides constraints on the timing of pluton emplacement and dike crystallization. Pluton emplacement ages can be compared with previously existing and new thermochronologic cooling ages to gain insight into the relative timing of magmatism and extension.

Foster et al. (2007) reported an Eocene granodiorite sheet in the central AMCC footwall, with a U-Pb age of 53 ± 0.6 Ma. This age is within the error of one of our samples from the south-central footwall (070518CH4) and is similar in age to the dike we sampled near the northern map area (071918CH7). These ages overlap with early-stage exhumation as determined in this study and by Foster et al. (2010), which reported $^{40}Ar/^{39}Ar$ cooling ages on mica that indicate the initiation of AMCC exhumation at 53 ± 1 Ma, with slip along the detachment lasting until at least 39 Ma. The only existing ages for the PCB (two-mica granite) are K-Ar biotite and muscovite ages that range from 54 to 49 Ma (Wallace et al., 1992). The K-Ar system has a closure temperature between 300 and 425°C (e.g., Grove & Harrison, 1996), so these ages likely record cooling of the PCB during the early stages of footwall exhumation. This timing of cooling falls within the

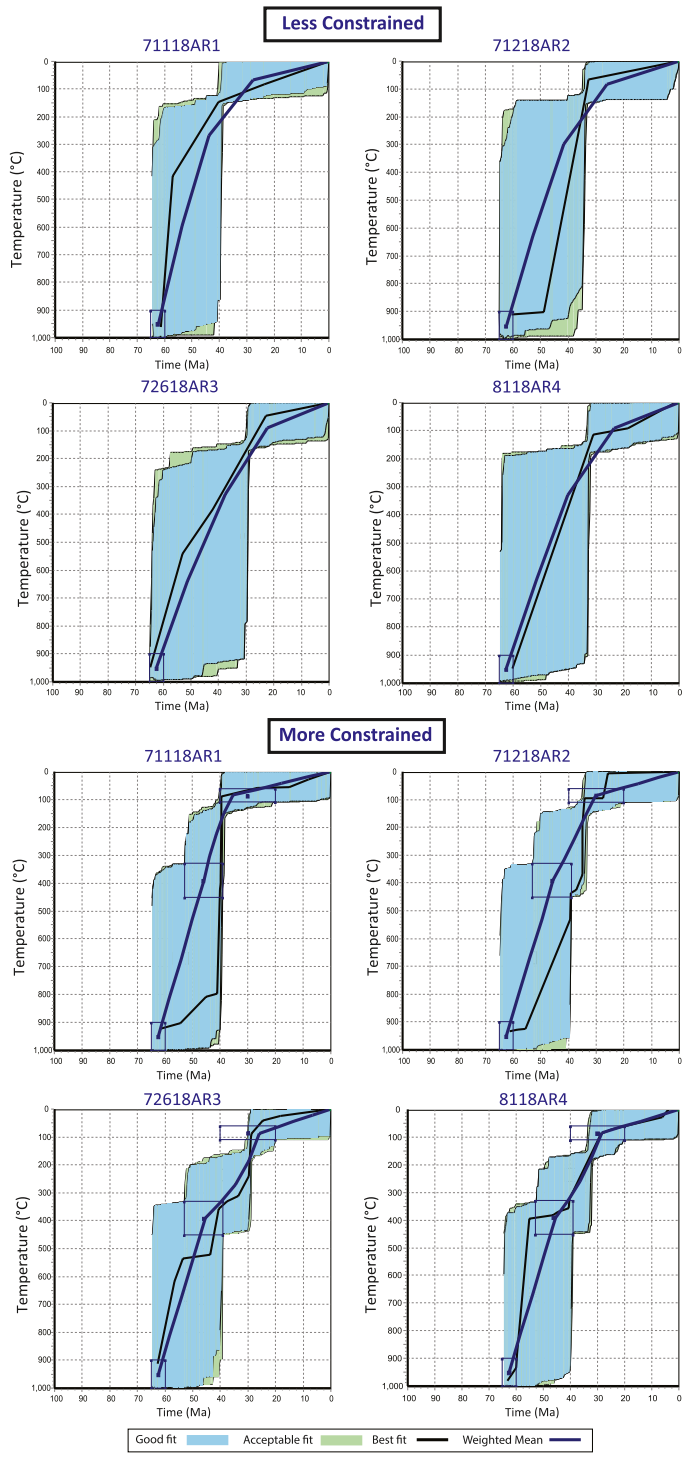

Figure 10. HeFTy model results for individual samples. Top: minimal constraints (U-Pb) crystallization ages, zircon He cooling ages, and surface temperature only to allow as much freedom as possible for modeled t-T paths. Bottom: five specific input constraints. (1) Zircon U-Pb crystallization ages indicate temperatures >900°C until 65–60 Ma. (2) $^{40}Ar/^{39}Ar$ Muscovite (450–350°C) and Biotite (380–330°C) recorded cooling ages between 53 and 39 Ma. (3) Zircon (U-Th)/He ages indicate cooling to 190–170°C from 42 to 25 Ma. (4) Apatite fission track (110–60°C) yielded ages between 40 and 20 Ma. (5) Samples were collected at the surface (20–0°C) at 0 Ma.

range of $^{40}Ar/^{39}Ar$ cooling ages produced by Foster et al. (2010) that we used as a constraint in our thermal modeling. The Paleocene (~61 Ma; Figure 7) U-Pb ages obtained in this study indicate that crystallization of the PCB began at least 7 Ma before the onset of extension.

The U-Pb ages obtained for the two-mica granites in this study are very complex, with the youngest 19 ages for sample 061218CH1 ranging from ~59 to ~74.5 Ma (Figures 7 and S1). The youngest 17 ages for sample 072018CH8 range from ~56 to ~76 Ma, with six Cretaceous ages (Figure 7). The Cretaceous ages present in both the samples are likely from zircons that were incorporated into two-mica melt from existing plutons (probably the Storm Lake pluton or equivalent; Foster et al., 2010; Wallace et al., 1992). The complex melting history of the two-mica granite is likely another reason that our MSWD values are higher than preferred (Figure 7). Despite this complexity, none of our individual grain ages are <56 Ma and our mean weighted averages (combined with field observations) indicate that a significant volume of two-mica granite was emplaced in the Paleocene, several million years before the onset of extension. The age complexity of the PCB warrants additional sample collection and geochronological analysis to ensure that our U-Pb ages are representative of the entire intrusive suite.

The U-Pb crystallization ages (~52.8, ~51.0, ~46.9 Ma) for three dikes within the AMCC footwall are all younger than the onset of extension at ~53 Ma (this study; Foster et al., 2010). These ages, combined with the observation of little to no deformation in the dikes, help to constrain the timing of initiation of AMCC exhumation. The fact that the host rocks (primarily two-mica granite) locally display greenschist-facies subsolidus foliation, and the dikes are relatively undeformed (Figures 6a–6c), suggests that the footwall must have cooled significantly between ~62 and 53 Ma. The lack of evidence for ductile deformation of quartz in the dikes may even suggest footwall cooling through 300–350°C before 53 Ma, although this is generally not in agreement with our time-temperature modeling results (Figure 10). Regardless, this field and geochronologic relationship suggests an initiation of exhumation that is consistent with that of Foster et al. (2010). The dikes in our field area are interpreted as synextensional magmatism that occurred during early- to mid-stage slip on the ADF. Synextensional igneous activity is common in MCCs, and both plutons and dikes can be emplaced as a response to decompression during exhumation (e.g., Lister & Baldwin, 1993; Whitney et al., 2013). It is well-documented that intrusive magmatism in MCC footwalls can lead to a decrease in crustal viscosity and strength through thermal advection, thereby triggering and/or facilitating exhumation (e.g., Konstantinou et al., 2013; Stevens et al., 2016). Thermal weakening and strain localization due to magmatism is expected to enhance MCC exhumation, particularly in regions that have an overthickened crust that has become gravitationally unstable (e.g., Coney & Harms, 1984).

Our U-Pb ages, thermochronology data, and time-temperature paths generated by HeFTy favor two-mica pluton crystallization at ~60 Ma followed by initial relatively rapid cooling through ~45 Ma at a rate of ~33°/m.y. (Figure 10). This phase of cooling is attributed to both cooling toward the ambient temperature of the host rocks and the earliest extension along the Anaconda detachment. Exhumation and associated magmatism, represented by synextensional dikes in the AMCC footwall and extrusive equivalents surrounding, indicate a second episode of significantly slower cooling (~16°/m.y.) due to exhumation and footwall unroofing along the Anaconda detachment from ~45 to 25 Ma. These values are consistent with the data obtained in this study, as well as $^{40}Ar/^{39}Ar$ and apatite fission track ages from Foster et al. (2010). All timing constraints taken together, we interpret that two-mica pluton emplacement predates Eocene extension along the south-central Anaconda detachment, acting as a driving factor for the formation of the AMCC rather than a response. Subsequent synextensional magmatism likely contributed to continued exhumation into the Cenozoic.

6.2. Lu-Hf Isotopes

An analysis of Lu-Hf isotopic ratios in igneous rocks provides information into the how "isotopically evolved" a melt was at the time of crystallization (e.g., Vervoort, 2014). In the Lu-Hf system, the daughter product prefers to partition into melt, which results in crustal rocks having relatively depleted Hf values. We refer to such crustal rocks as being "evolved," while referring to melts that have recently been derived from the mantle as "juvenile" (e.g., Chapman et al., 2017; Vervoort et al., 1999). When paired with U-Pb geochronology ages, Lu-Hf isotopic ratios can be used to gain insight into the magmatic evolution of a region that has experienced multiple episodes of igneous activity (e.g., Gaschnig et al., 2011). This pairing technique

of U-Pb and Lu-Hf (as well as with Sr-Rb, Sm-Nd, etc.) has been applied to rocks in Cordilleran orogenic systems around the world (e.g., Balgord et al., 2021; Chapman et al., 2017).

Trends in Lu-Hf signatures are not well studied for the plutons and dikes exposed in western Montana. However, various radio-isotopic systems have been used to investigate the evolution of the Idaho batholith and Challis intrusions of eastern Idaho, which lie ~100 km west of the AMCC (Gaschnig et al., 2011). One of the isotopic trends observed in the Idaho batholith is a steady decrease in εHf values from −8 εHf at ~90 Ma to ~−25 εHf at ~50 Ma (Figure 8), which has been interpreted as progressive crustal thickening and incorporation of more crust into rising arc magmatism (Gaschnig et al., 2011). εHf values in the subsequent Challis Intrusives (~48 Ma) display much more juvenile εHf values, ranging from −28 to −3 with an average around −11 (Figure 8; Gaschnig et al., 2011). The influx of magmatism with relatively juvenile εHf values ("isotopic pull-up") is interpreted to reflect a major regional shift to extensional tectonics in the western United States (e.g., Armstrong & Ward, 1991; Gaschnig et al., 2011).

Our new Lu-Hf data for two igneous samples obtained from the AMCC footwall and one detrital sample collected from within the AMCC supradetachment basin (Howlett & Laskowski, 2021) reflect a nearly identical trend in εHf space (Figure 8). The detrital grains—collected from the reworked Miocene conglomerate known as the Cabbage Patch Formation—are hypothesized to have been sourced primarily from the Late Cretaceous Royal Stock in the northern Flint Creek Range, ~60 km along-strike to the northeast of this map area (Howlett & Laskowski, 2021; Loen, 1994; O'Neill et al., 2004). Having been eroded from the footwall of the AMCC, the εHf values of these detrital grains can be plotted alongside the two other igneous samples obtained from the field area of this study (Figure 8). The detrital grains sourced from the northern Flint Creek AMCC footwall range from ~83 to ~68 Ma and display a clear decrease in εHf value as they get younger (Figure 8). The younger, ~61 Ma two-mica granite continues this isotopic trend of increasingly enriched Hf values with time (Figure 8). Finally, the youngest dike dated using U-Pb geochronology (071118CH5) is plotted in εHf space and shows a remarkably similar "pull-up" to that seen in the Challis Intrusives of Gaschnig et al. (2011) (Figures 5 and 8).

It has been recognized that the more juvenile Hf values in the mid-Eocene Challis Intrusives are likely a result of increased mantle input, but the specific cause for the increase remains unclear (e.g., Gaschnig et al., 2011). Trace element and Pb isotopic data have been used to argue that the lithospheric mantle beneath eastern Idaho and western Montana may have melted, but whether the melting was due to decompression associated with extension or the influx of hot asthenosphere has not been established (McKervey, 1998; Norman & Mertzman, 1991). Considering that the pull-up in Hf value overlaps in space and time with widespread magmatism containing T/REE and isotopic signatures characteristic of heating of a hydrated lithospheric mantle (e.g., Feeley, 2003; Humphreys, 2009), we suggest that the increase in εHf values for the synextensional dike in the AMCC footwall is a result of dynamic removal of the shallow Farallon slab. This removal resulted in asthenospheric upwelling, heating of low-mid crust, elevation of the geotherm, and ultimately facilitated the initiation of MCC exhumation (Figure 11), an interpretation expanded upon in the following section.

We acknowledge that while the Hf data are compatible with the tectonic scenario presented above and in the following sections, they do not require it. In the Albion-Raft River-Grouse Creek MCC (ARG) of northern Utah, for example, εHf values decrease continuously during MCC exhumation, despite slab removal and mantle-driven magmatism being the preferred trigger of extension initiation (e.g., Konstantinou et al., 2013). The different εHf trends seen in the ARG and AMCC are likely the result of each region's differing magmatic history. In the region surrounding the AMCC, ~50 Myr of arc magmatism prior to MCC formation depleted the lower continental lithosphere and increased the proportion of crustal melt over time, reflected by increasingly evolved εHf values during the Mesozoic. Subsequent slab removal and addition of mantle basalts to a depleted lower lithosphere was reflected quickly in the isotopic signatures (Figure 8). This contrasts with the magmatic history in the ARG, where the ~42 Ma magmatism is the first major magmatic event since the Proterozoic (e.g., Konstantinou et al., 2013). The absence of prolonged magmatism preceding slab removal in this region likely resulted in mantle input being confined to the lower crust; as such, the increased mantle component is not reflected as prominently in εHf space during MCC exhumation (Konstantinou et al., 2013; pers. comm). As a result of the non-uniqueness of Lu-Hf isotopic data, additional sample collection and geochemical modeling are necessary to conclusively determine whether the

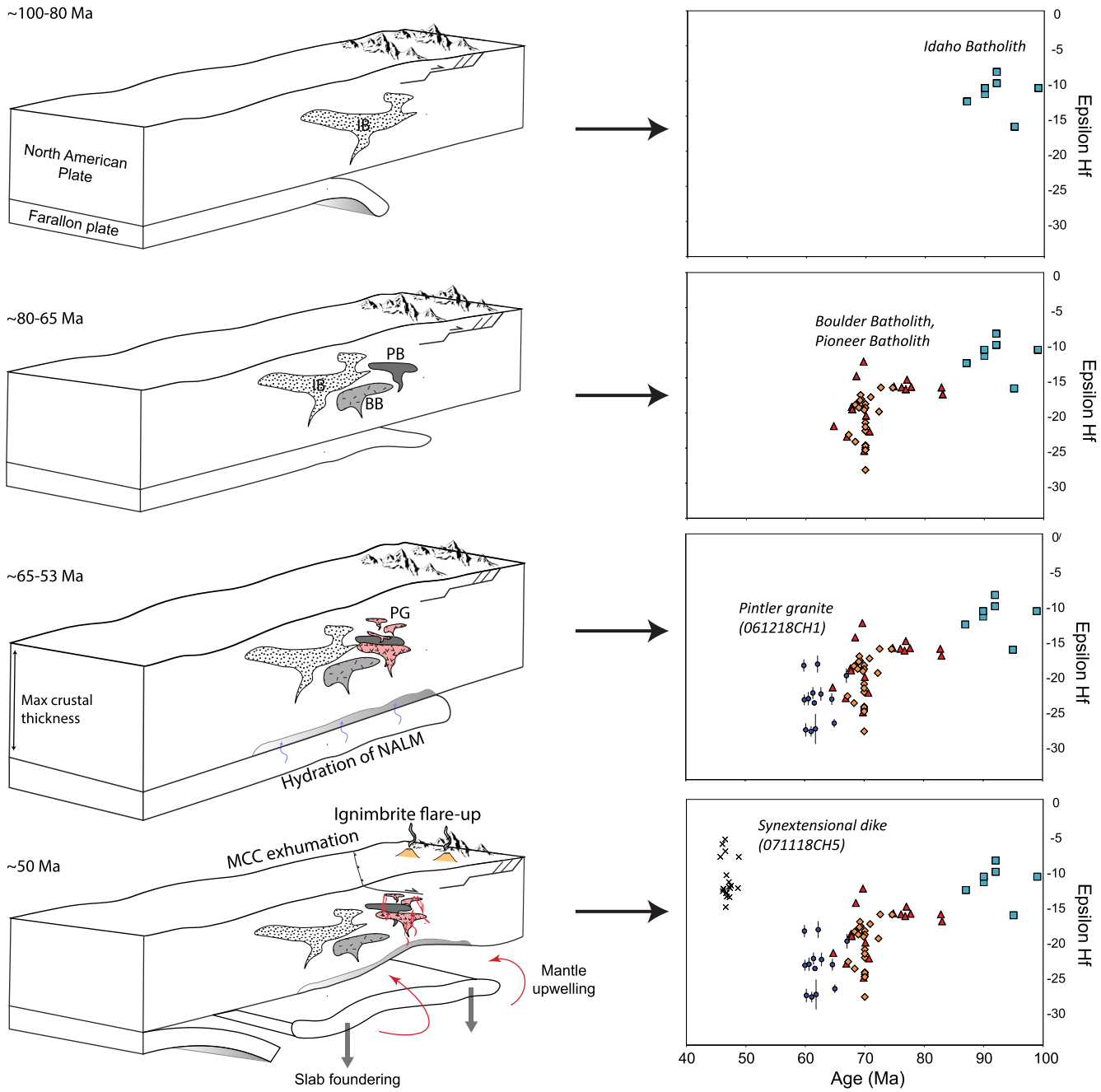

Figure 11. Schematic tectonic model to explain the systematic changes observed in εHf space over time in the Anaconda metamorphic core complex (AMCC) footwall. Increasingly evolved εHf values from 100 to 60 Ma represent crustal thickening and incorporation of a larger crustal component into melt. The subsequent pull up in Hf space seen in synextensional footwall dike likely represents increased mantle input due to slab removal, which elevated geotherms, triggered ignimbrite flare-up volcanism, and facilitated large-magnitude extension in the upper plate. Contemporaneous exhumation of Bitteroot MCC omitted for clarity. NALM, North American lithospheric mantle.

pull-up in Hf space in the northern Cordillera is a result of mantle upwelling due to slab removal or some other mechanism such as primary melting entirely within the lithospheric mantle due to crustal thickening (e.g., Norman & Mertzman, 1991).

It is noteworthy that Sm-Nd isotopic data from the nearby Lowland Creek volcanic field (LCVF) partially overlap in time and isotopic space with sample 071118CH5 (Dudás et al., 2010). This supports the interpretation that the LCVF is the surficial expression of magmatic activity that occurred in the footwall of the

AMCC during exhumation. The LCVF was active from 52.9 to 48.6 Ma (Dudás et al., 2010), initiating within the error of when slip along the Anaconda detachment began (Foster et al., 2010; this study). As part of the widespread volcanism of the northern Cordilleran segment of the ignimbrite flare up, the temporal overlap suggests a linkage between the two (Feeley, 2003).

6.3. Tectonic Evolution of the AMCC

The AMCC, as part of the northern belt of MCCs in the western United States (Figure 1), is situated in the hinterland of the Cordilleran fold-thrust belt (e.g., Coney & Harms, 1984). Core complexes in this region are the oldest in the North American Cordillera, with exhumation beginning in the Eocene between 50 and 55 Ma (Foster et al., 2001, 2007, 2010). The early Eocene onset of exhumation determined in the AMCC (~53 Ma; Foster et al., 2010) fits into this time frame and corresponds with an episode of large-magnitude extension that began along the previously thickened Sevier hinterland at ~55 Ma (Constenius, 1996; Foster et al., 2001). In the ~45 Myr leading up to the onset of this extension episode (~100–55 Ma), both arc magmatism and eastward propagation of the fold and thrust belt led to extensive crustal thickening in eastern Idaho and western Montana (e.g., DeCelles, 2004; DeCelles & Graham, 2015; O'Neill et al., 2004). Spatially and temporally overlapping arc-magmatism included the emplacement of the Idaho batholith (~90 Ma) and the Boulder, Pioneer, and Tobacco Root batholiths (~75–80 Ma), all of which contributed significant mass to the orogenic wedge (e.g., Foster et al., 2012; Gaschnig et al., 2011; Lageson et al., 2001). Our U-Pb geochronology ages from the PCB support the interpretation that Paleocene plutonism contributed additional heat and mass to the already hot and overthickened Cordilleran lithosphere (e.g., Coney & Harms, 1984) prior to the onset of extension at ~53 Ma (Foster et al., 2010; this study). It is proposed that these final pulses of magmatism in the northern Cordillera hinterland thermomechanically and gravitationally weakened the crust, priming it for the formation of the Bitterroot and AMCCs.

The initiation of large-magnitude extension in the northern Cordillera subsequent to thrust faulting and extensive pluton emplacement was contemporaneous with widespread volcanism of the Challis-Absaroka-Colville-Kamloops-Bitterroot-Lowland Creek-Montana alkalic province, which lasted from 53 to 45 Ma (Breitsprecher et al., 2003; du Bray et al., 2006; Dudás et al., 2010; Feeley, 2003; Feeley et al., 2002; Foster & Fanning, 1997; Foster et al., 2001, 2010; House et al., 2002; Morris et al., 2000). The spatio-temporal overlap of this volcanism with extension in the upper plate necessitates a tectonic model that explains both (e.g., Foster et al., 2010). Several mechanisms have been proposed to explain this widespread volcanism, including subduction and/or removal of the Farallon slab (e.g., Armstrong et al., 1977; Schmandt & Humphreys, 2011), a slab window (Breitsprecher et al., 2003), and regional extension (Morris et al., 2000). Previous isotopic and trace element analyses suggest that these volcanics were derived from partial melting of a mantle lithosphere that had been hydrated during the Mesozoic by an underlying oceanic slab (e.g., Feeley, 2003).

Dynamic removal of the subducted Farallon slab has been proposed as a cause of extension and volcanism in the northern MCC belt, as exposure of a refrigerated and metasomatized lower crust to upwelling asthenosphere would naturally cause both (Humphreys et al., 2003). The exact mechanism by which the slab was removed remains a topic of discussion. Dickinson (2002) suggested that a north-to-south rollback of the Farallon slab could explain the evolution of volcanism, but it has been pointed out that a simple steepening of the slab by rollback has difficulty explaining the contemporaneous nature of Eocene volcanism over a broad region in the northern Cordillera (e.g., Feeley, 2003). A simple rollback model has also been questioned due to the limited velocity with which a slab can push through the underlying asthenosphere (Kincaid & Olson, 1987; Tao & O'Connell, 1992). An additional problem with some suggested slab removal mechanisms in the northern Cordillera is that they do not take into account the complexities of the accretion of Siletzia, a fragment of Farallon lithosphere that filled the Columbia Embayment in the Eocene (Schmandt & Humphreys, 2011; R. E. Wells et al., 2014). Considering all the above, Humphreys (1995, 2009) and Schmandt and Humphreys (2011) propose that a portion of the shallow Farallon slab was removed due to foundering that occurred as a result of Siletzia accretion at ~55 Ma. This model suggests that following main-phase Cretaceous arc magmatism (i.e., Idaho and Boulder batholiths), the east-northeastward subducting Farallon slab flattened against the base of the northern Cordillera. This interpretation is supported by a lull in arc magmatism that coincided with Laramide-style thrusting in the early Eocene (Feeley, 2003; van der

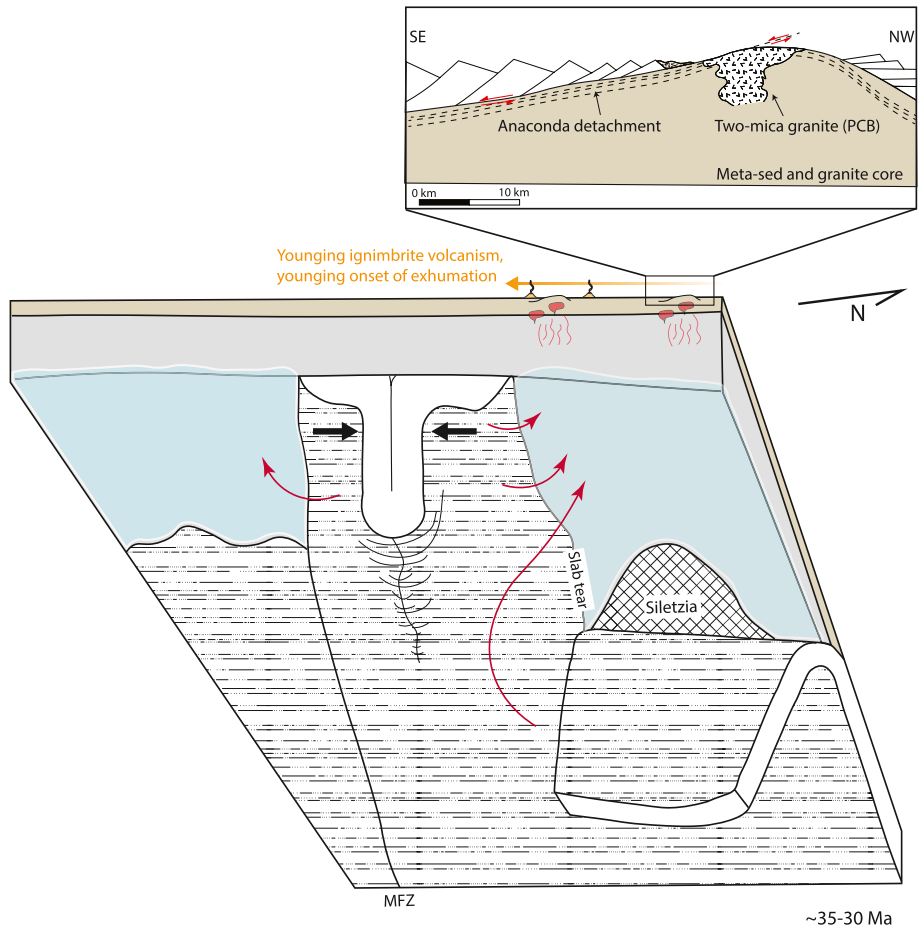

Figure 12. Late stage of the Farallon slab bucking model for Anaconda metamorphic core complex (AMCC) formation (modified from Humphreys, 1995). Following the accretion of Siletzia lithosphere at ~55 Ma in the northern Cordillera, the flat Farallon slab beneath Idaho and western Montana foundered and exposed the hydrated base of the continental lithosphere (blue regions) to upwelling asthenosphere (red arrows). Foundering of the slab from beneath the northern Cordillera (omitted for clarity) and the establishment of a more steeply dipping slab beneath western NA resulted in a tearing or necking separation of Farallon slab at the approximate latitude of the AMCC, enabling southward buckling. Bold black arrows represent buckling direction. Explanation for the migration of volcanism south of the Great Basin is detailed in Humphreys (1995). MFZ, Mendocino Fracture Zone. MCCs not to scale.

Pluijm et al., 2006). The subsequent accretion of Siletzia oceanic lithosphere at 55 Ma resulted in the establishment of the relatively steep dipping Cascadia subduction zone on its western side (Figure 12; Schmandt & Humphreys, 2011; R. E. Wells et al., 1984). Shortly after Siletzia accretion, foundering of the Farallon slab and upwelling of asthenosphere beneath northwestern North America led to the isotopically juvenile magmatic flare-up that spanned from southern British Columbia to the region surrounding the AMCC (e.g., Feeley, 2003; Gehrels et al., 2009; this study). This mechanism of Farallon slab removal is most consistent with regional geophysical, geochemical, geologic data (Dudás et al., 2010; Feeley, 2003; Foster et al., 2010; Schmandt & Humphreys, 2011; this study) surrounding the AMCC and the northwestern Cordillera and is our preferred model for the onset of the ignimbrite flare-up. Other recent work has provided younger estimates for the timing of Siletzia accretion, between 50.5 and 45 Ma (R. E. Wells et al., 2014). This timing still overlaps with a majority of the widespread volcanism in the northern Cordillera but would not explain the >50 Ma onset of the ignimbrite flare-up in western Montana. Thus, it is possible that some component of rollback and/or foundering of the Farallon slab occurred prior to the accretion of Siletzia.

A compilation of geological, geochronological, and thermochronological data in the northern Cordillera reveals that rates of MCC extension generally decrease from southern Canada to the Pioneer MCC of central Idaho (Vogl et al., 2012). Consistent with our preferred model, these authors suggest that these differing

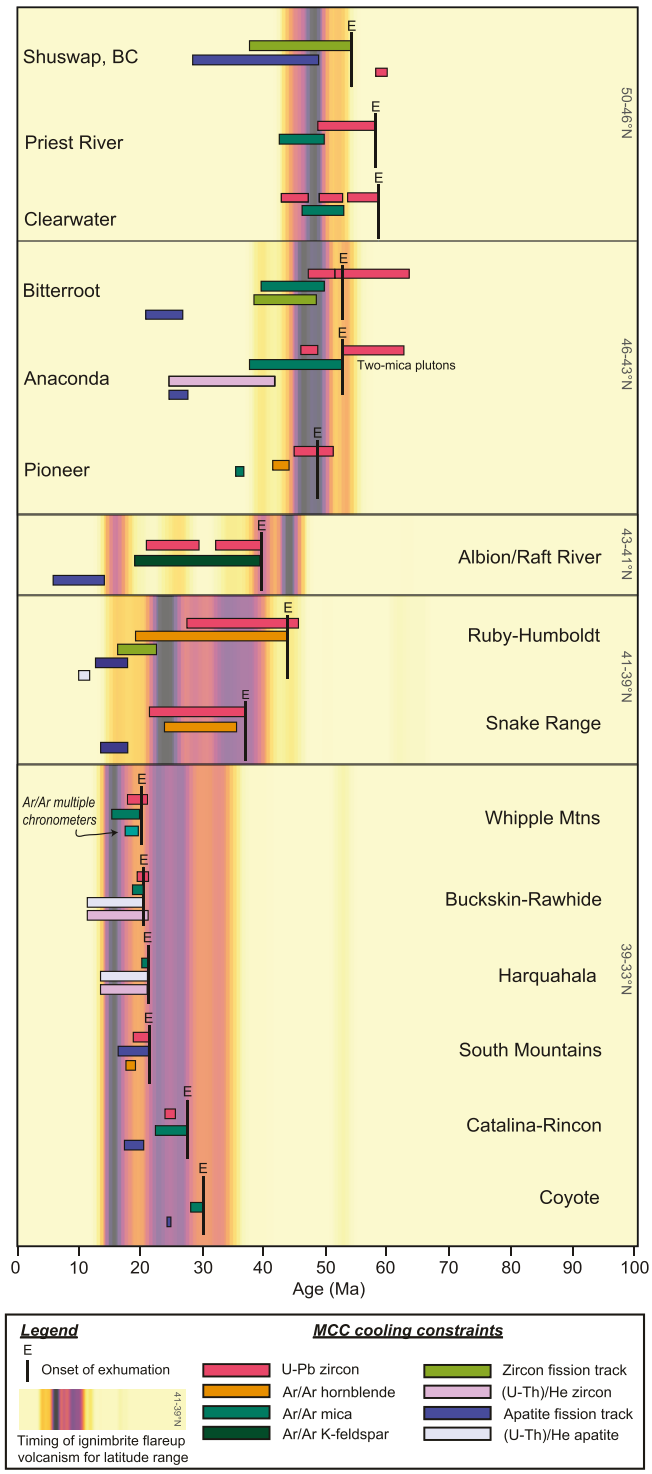

Figure 13. Timing comparison of metamorphic core complex (MCC) footwall cooling and ignimbrite flare-up volcanism from north to south in the North American Cordillera. Probability density plots for volcanic ages are visualized as "heatmaps," with darker colors representing distribution peaks. See Table 3 for detailed age constraints and references for each MCC.

rates could be explained by a change in subduction zone geometry from relatively steep in the northern Cordillera to shallow at approximately the latitude of the Snake River Plain (Vogl et al., 2012). Other possible explanations for the differing extension rates (as well as the cause of magmatic evolution) include oblique subduction of the Kula or Resurrection plate (e.g., Engebretson et al., 1985; Fuston & Wu, 2020; Madsen et al., 2006), differences in the size and thermal state of the orogenic wedge (e.g., Beaumont et al., 2006), and/or the creation of a slab window due to subduction of the Farallon/Kula or Farallon/Resurrection ridge (Breitsprecher et al., 2003).

Some researchers have suggested that the localization of northern belt MCCs along the craton margin rules out slab removal, and that the confinement of MCCs to the crust makes them insensitive to slab dynamics at depth (e.g., Stevens et al., 2017). In contrast, we interpret that the pull up in εHf space that coincides with AMCC footwall cooling (~46 Ma; Figures 9 and 13) represents an influx of asthenospheric mantle into space created by Farallon removal (e.g., Gaschnig et al., 2011). If the AMCC footwall were not sensitive to Farallon slab dynamics, we would not expect to see this abrupt input of juvenile melt into the crust. Furthermore, geochemical and thermomechanical modeling on core complexes of the Bering Strait region and northern Basin and Range have concluded that mantle-derived magmatism plays an essential role in partial melting, pluton emplacement, and MCC formation (Amato & Miller, 2004; Gans et al., 1989; Konstantinou et al., 2013). Therefore, it is crucial to consider the role of sublithospheric processes such as slab removal into future theoretical and computational modeling of core complex formation. Regardless of the exact mechanism of Farallon slab removal, it appears that deep lithospheric processes play an important role in the generation of MCC footwall magmas, evolution of Cenozoic volcanism, and general development of core complexes in the northern Cordillera.

6.4. Ignimbrite Flareup Volcanism and MCC Formation in the Western United States

An additional reason that the buckling model of Humphreys (1995) is our preferred mechanism of slab removal is because it explains the widespread volcanism in the northern Cordillera while also providing an explanation for the subsequent migration of the ignimbrite flare-up from north to south across the Great Basin. At the time of Siletzia accretion in the northern Cordillera, continued quiescence in the Sierra Nevada arc and a general lack of magmatic activity in the great basin suggests that the Farallon plate was still flat south of the southern margin of Siletzia (Schmandt & Humphreys, 2011). The reconfiguration of Farallon lithosphere in the northern Cordillera and foundering of the flat slab resulted in a tear and/or necking separation at approximately the latitude of the AMCC. Once the tear was established, the flat slab to the south buckled and its northern edge propagated to the south (Figure 12; Humphreys, 1995, 2009). Southward propagation of the slab tear due to buckling progressively exposed the base of western North America to upwelling asthenosphere and may explain the north to south migration of calc-alkaline volcanism of the ignimbrite flare-up across the Great Basin (Figure 12; Humphreys, 1995; Schmandt & Humphreys, 2011). Several compilations have revealed the along-strike variability in the timing of MCC exhumation (e.g., Armstrong & Ward, 1991; Dickinson, 2002; Vogl

Table 3
Timing of Exhumation for Selected Metamorphic Core Complexes (MCCs) in the North American Cordillera

MCC belt	Core complex	Geo/thermochronologic constraints on exhumation[a]	References
Northern	Shuswap	54–38 Ma (ZFT); 49–28 Ma (AFT)	Lorencak et al. (2001); Vanderhaeghe et al. (2003)
	Priest River	58–48 Ma (U-Pb); 50–43 Ma (^{40}Ar/^{39}Ar bio/musc, K-Ar bio)	Stevens et al. (2016); Doughty and Price (1999)
	Clearwater	59–55 Ma (U-Pb zir); 54–47 Ma (^{40}Ar/^{39}Ar mica)	Doughty et al. (2007)
	Bitterroot	53–48 Ma (U-Pb zir); 50–40 (^{40}Ar/^{39}Ar bio/musc/kfeld); 48–39 Ma (ZFT) 26–22 Ma (AFT)	Foster and Raza (2002)
	Anaconda	53–38 Ma (^{40}Ar/^{39}Ar bio); 42–25 Ma (ZHe) 28–25 Ma (AFT)	Foster et al. (2010); this study
Central	Pioneer	52–46 (U-Pb zir); 45–43 Ma (^{40}Ar/^{39}Ar hbl); 37–36 Ma (^{40}Ar/^{39}Ar bio); 37–36 Ma (^{40}Ar/^{39}Ar kfeld)	Silverberg (1990); Vogl et al. (2012)
	Albion/Raft-River	41–20 Ma (^{40}Ar/^{39}Ar kfeld); 37.5–22 Ma (U-Pb zir) 13.5–7 Ma (AFT)	Lee et al. (2017); Konstantinou et al. (2012, 2013); M. L. Wells et al. (2000)
	Ruby-Humboldt	45–20 Ma (^{40}Ar/^{39}Ar hbl); 23.5–12.1 Ma (ZFT); 18.5–14.2 Ma (AFT); 12–10 Ma (AHe)	Snoke et al. (1997); MacCready et al. (1997); Colgan et al. (2010); Mueller (2019)
	Snake	36–25 Ma (^{40}Ar/^{39}Ar hbl); 37.8–22.5 Ma (U-Pb zir); 19–15 Ma (AFT)	Miller et al. (1988, 1999); Lee et al. (2017)
Southern	Whipple	22–18 Ma (U-Pb zir); 20.5–18.5 Ma (^{40}Ar/^{39}Ar groundmass, bio, hbl); 21–15 Ma (^{40}Ar/^{39}Ar kfeld); 21.5 Ma (onset) (AHe/ZHe);	Gans and Gentry (2016); Foster and John (1999); Stockli et al. (2006)
	Buckskin-Rawhide	21 Ma (U-Pb zir); 22–12 Ma (ZHe); 21–12 Ma (AHe); 21–19 Ma (^{40}Ar/^{39}Ar kfeld)	Singleton et al. (2014); Scott et al. (1998)
	Harquahala	21–14 Ma (ZHe/AHe); 21.4–20 Ma (^{40}Ar/^{39}Ar bio)	Prior et al. (2016); Richard et al. (1990)
	South Mountains	22 Ma (U-Pb zir); 20.7 Ma (^{40}Ar/^{39}Ar hbl); 20.3 Ma (^{40}Ar/^{39}Ar hbl); 22–17.5 Ma (AFT)	Fitzgerald et al. (1993); Reynolds et al. (1986)
	Catalina-Rincon	28–23 Ma (^{40}Ar/^{39}Ar bio/kfeld); 26–25 Ma (U-Pb zir); 21.4–18.8 (AFT)	Terrien (2012); Fayon et al. (2000); Ducea et al. (2020)
	Coyote	31–29 Ma (^{40}Ar/^{39}Ar bio/musc); 24 Ma (AFT)	Gottardi et al. (2020)

[a]Key for technique abbreviations: AFT, apatite fission track; AHe, apatite (U-Th)/He; bio, biotite; hbl, hornblende; kfeld, potassium feldspar; musc, muscovite; ZFT, zircon fission track; ZHe, zircon (U-Th)/He; and zir, zircon.

et al., 2012), and it has been suggested that there is a spatio-temporal overlap between the migration of volcanism and MCC formation in the upper plate. This possible relationship justifies an updated compilation containing modern thermochronological constraints on the timing of footwall exhumation for different MCCs.

In order to constrain the relationship between the ignimbrite flare-up and Cenozoic MCC formation, we compiled age and geochemical data from the North American Volcanic and Intrusive Rock Database (NAVDAT) database for Cenozoic volcanics associated with the ignimbrite flare-up. To track the migration of volcanism during the Cenozoic, the western United States was compartmentalized into five regions based on latitude: 50–46°N, 46–43°N, 43–41°N, 41–39°N, and 39–33°N (for more detailed description of compilation parameters, see Text S1 and Figure S2). Probability density plots for the extracted volcanics, displayed as "heat maps" (Sharman et al., 2018), were plotted beneath an updated compilation of thermochronology cooling ages for major MCC footwalls (Table 3 and Figure 13). This visualization confirms that there is a pronounced spatio-temporal relationship between the migration of ignimbrite flare-up magmatism and the initiation of MCC exhumation in some regions (Figure 13). Based on our analysis, it appears that in many cases (including in the AMCC and Bitterroot MCC), the onset of extension coincides with or is subsequent to the onset of ignimbrite volcanism. Similar relationships observed in the central and southern MCC belts

support previous hypotheses that flare-up magmatism and volcanism, which we interpret to be intimately linked to the removal of the shallowly subducted Farallon slab, served as a contributing force for core complex formation from the Paleocene-Miocene in the western United States (e.g., Armstrong & Ward, 1991; Coney & Harms, 1984). Exceptions to this relationship, such as those observed in the Priest River and Clearwater MCCs where the onset of extension precedes that of the ignimbrite flare-up, could be explained by a number of phenomena. One possibilty is that other driving forces such as gravitational collapse or regional extension controlled the onset of extension in these locations. Another possibility is that variability in the quality and precision of volcanic ages extracted from the NAVDAT database, or a general lack of data available, lead to the variable relationship observed between ignimbrite volcanism and extension. It is also noteworthy that several researchers have used thermobarometry results to conclude that some MCCs (e.g., Snake Range) experienced an earlier phase of exhumation in the Late Cretaceous (e.g., Cooper et al., 2010; Lee et al., 2017; M. L. Wells & Hoisch, 2008). We omit this earlier phase from our compilation (Figure 13) as it is generally not considered part of the post-Laramide phase of MCC formation and is not definitively recorded along the entire strike of the North American Cordillera. Regardless of the uncertainty above, we acknowledge that each individual MCC has a complex history and that localized sample targeting and high-resolution geo- and thermochronology is necessary to understand this relationship in detail.

In southern Arizona, the sweep of the ignimbrite flare-up occurred from southeast to northwest, which contrasts to the north to south migration seen across the Great Basin (e.g., Best et al., 2016). The migration of volcanism in the southern Basin and Range is represented by ages decreasing from the area surrounding the Catalina-Rincon MCC to the region around the Whipple Mountains MCC (Figure S3; e.g., Coney & Reynolds, 1977). This migration is explained in the buckling model to be a result of northwestward propagation of the Mendocino fracture zone (e.g., Severinghaus & Atwater, 1990) and/or small-scale convection (drip removal) of lithospheric mantle beneath the region (Humphreys, 1995). West-northwest directed slab rollback is also a possibility (e.g., Bahadori & Holt, 2019; Coney & Reynolds, 1977). The exact mechanism of slab removal in the southern Basin and Range is beyond the scope of this manuscript; however, our compilation of thermochronologic constraints for the southern belt of MCCs shows a southeast to northwest younging in the onset of exhumation (Figure 13), which is consistent with the interpretation that slab removal played a role in MCC formation in the southern Basin and Range region as well. Data from several MCCs in northern Mexico (e.g., Sierra Mazatan, Aconchi) are not included in our compilation because they exist south of the area that experienced the ignimbrite flare-up. That said, recent studies from this region confirm a younger-to-the-northwest trend for the onset of MCC exhumation (Gottardi et al., 2018, 2020; Wong & Gans, 2008; Wong et al., 2010).

7. Conclusions

The results of this integrated geologic, geochronologic, and thermochronologic study of the AMCC of western Montana suggest that it is an example of a core complex whose development was primed by retroarc thrust faulting and voluminous magmatism. These processes served to thicken and thermally weaken the crust, respectively. Following ~50 Myr of inboard arc magmatism in the northern Cordillera, Paleocene two-mica granites were emplaced in the future AMCC footwall. Following granite emplacement, extension along the Anaconda detachment began (~53 Ma; Foster et al., 2010; this study), coincident with the onset of explosive and laterally extensive ignimbrite flare-up volcanism. New zircon (U-Th)/He cooling ages ranging from ~48 to 25 Ma, combined with field observations, suggest that extension along the ADF lasted at least into the Oligocene.

The overlap between the onset of extension and widespread regional volcanism with a mantle origin (e.g., Feeley, 2003) supports dynamic lower plate processes as an initiating force of exhumation in the AMCC. Lu-Hf isotopic data from the Idaho batholith and AMCC are compatible with a tectonic scenario in which the flat Farallon slab foundered from beneath the northern Cordillera following the accretion of Siletzia at ~55 Ma (Schmandt & Humphreys, 2011). The subsequent removal of the flat slab from beneath the Great Basin due to slab buckling is consistent with regional geologic, geochemical, and geophysical data (e.g., Humphreys, 2009), and likely allowed asthenospheric mantle heating of a hydrated continental lithosphere, ultimately resulting in the migration of magmatism, elevation of geotherms, and development of MCCs in the upper plate. Our updated compilation of thermochronology cooling ages for MCC footwalls

corroborates previous evidence that there is a spatio-temporal overlap between the onset of ignimbrite flare-up volcanism and the initiation of MCC exhumation in the western United States.

Data Availability Statement

Tables S1–S3, containing igneous zircon U-Pb/Hf and zircon (U-Th/He) data sets are available in the supporting information for this paper, alongside supplementary text and figures referenced in main text. U-Pb and (U-Th)/He data are also available to the public online (https://www.geochron.org/dataset/html/geochron_dataset_2021_01_07_s2ObQ).

Acknowledgments
The authors express their gratitude to our colleagues at the Montana Bureau of Mines and Geology—especially Colleen Elliott. This manuscript benefited from conversations with Devon Orme, Dave Lageson, and Chance Ronemus. Alexandros Konstantinou is thanked for enlightening discussions surrounding geochemical trends observed in MCC footwalls. Scott Johnston, John Singleton, an anonymous reviewer, and associate editor Robinson Cecil provided detailed reviews that improved the paper. Margi Rusmore is appreciated for editorial handling. This research was supported by the USGS EDMAP cooperative agreement G18AC00143, NSF EAR-1649254 to the Arizona Laserchron Center, and the Geological Society of America graduate student research grants to C. Howlett and A. Reynolds.

References

Amato, J. M., & Miller, E. L. (2004). Geologic map and summary of the evolution of the Kigluaik Mountains gneiss dome, Seward Peninsula, Alaska. In D. L. Whitney, C. Teyssier, & C. S. Siddoway (Eds.), *Gneiss domes in orogeny*. Geological Society of America. https://doi.org/10.1130/0-8137-2380-9.295

Armstrong, R. L. (1982). Cordilleran metamorphic core complexes—From Arizona to Southern Canada. *Annual Review of Earth and Planetary Sciences*, *10*(1), 129–154. https://doi.org/10.1146/annurev.ea.10.050182.001021

Armstrong, R. L., Taubeneck, W. H., & Hales, P. O. (1977). Rb-Sr and K-Ar geochronometry of Mesozoic granitic rocks and their Sr isotopic composition, Oregon, Washington, and Idaho. *GSA Bulletin*, *88*(3), 397–411. https://doi.org/10.1130/0016-7606(1977)88<397:RAKGOM>2.0.CO;2

Armstrong, R. L., & Ward, P. (1991). Evolving geographic patterns of Cenozoic magmatism in the North American Cordillera: The temporal and spatial association of magmatism and metamorphic core complexes. *Journal of Geophysical Research*, *96*(B8), 13201–13224. https://doi.org/10.1029/91JB00412

Bahadori, A., & Holt, W. E. (2019). Geodynamic evolution of southwestern North America since the Late Eocene. *Nature Communications*, *10*(1), 5213. https://doi.org/10.1038/s41467-019-12950-8

Bahadori, A., Holt, W. E., & Rasbury, E. T. (2018). Reconstruction modeling of crustal thickness and paleotopography of western North America since 36 Ma. *Geosphere*, *14*(3), 1207–1231. https://doi.org/10.1130/GES01604.1

Balgord, E. A., Yonkee, W. A., Wells, M. L., Gentry, A., & Laskowski, A. K. (2021). Arc tempos, tectonic styles, and sedimentation patterns during evolution of the North American Cordillera: Constraints from the retroarc detrital zircon archive. *Earth-Science Reviews*, *216*, 1–34. https://doi.org/10.1016/j.earscirev.2021.103557

Beaumont, C., Nguyen, M. H., Jamieson, R. A., & Ellis, S. (2006). Crustal flow modes in large hot orogens. In R. D. Law, M. P. Searle, & L. Godin (Eds.), Channel flow, ductile extrusion and exhumation in continental collision zones (Vol. 268, pp. 91–145). Geological Society, London, Special Publications. https://doi.org/10.1144/gsl.sp.2006.268.01.05

Best, M. G., & Christiansen, E. H. (1991). Limited extension during peak Tertiary volcanism, Great Basin of Nevada and Utah. *Journal of Geophysical Research*, *96*(B8), 13509–13528. https://doi.org/10.1029/91JB00244

Best, M. G., Christiansen, E. H., de Silva, S., & Lipman, P. W. (2016). Slab-rollback ignimbrite flareups in the southern Great Basin and other Cenozoic American arcs: A distinct style of arc volcanism. *Geosphere*, *12*(4), 1097–1135. https://doi.org/10.1130/GES01285.1

Bird, P. (1988). Formation of the Rocky Mountains, Western United States: A continuum computer model. *Science*, *239*(4847), 1501–1507. https://doi.org/10.1126/science.239.4847.1501

Breitsprecher, K., Thorkelson, D. J., Groome, W. G., & Dostal, J. (2003). Geochemical confirmation of the Kula-Farallon slab window beneath the Pacific Northwest in Eocene time. *Geology*, *31*(4), 351–354. https://doi.org/10.1130/0091-7613(2003)031<0351:gcotkf>2.0.co;2

Carrapa, B., DeCelles, P. G., & Romero, M. (2019). Early inception of the laramide orogeny in southwestern Montana and northern Wyoming: Implications for models of flat-slab subduction. *Journal of Geophysical Research: Solid Earth*, *124*(2), 2102–2123. https://doi.org/10.1029/2018JB016888

Cassel, E. J., Smith, M. E., & Jicha, B. R. (2018). The impact of slab rollback on Earth's surface: Uplift and extension in the hinterland of the North American Cordillera. *Geophysical Research Letters*, *45*(20). https://doi.org/10.1029/2018GL079887

Chapman, J. B., Ducea, M. N., Kapp, P., Gehrels, G. E., & DeCelles, P. G. (2017). Spatial and temporal radiogenic isotopic trends of magmatism in Cordilleran orogens. *Gondwana Research*, *48*, 189–204. https://doi.org/10.1016/j.gr.2017.04.019

Christiansen, R. L., Yeats, R. S., Graham, S. A., Niem, W. A., Niem, A. R., & Snavely, P. D. (1992). Post-Laramide geology of the U.S. Cordilleran region. In B. C. Burchfiel, P. W. Lipman, & M. L. Zoback (Eds.), *The Cordilleran orogen* (p. 261-R-111). Geological Society of America. https://doi.org/10.1130/DNAG-GNA-G3.261

Colgan, J. P., Howard, K. A., Fleck, R. J., & Wooden, J. L. (2010). Rapid middle Miocene extension and unroofing of the southern Ruby Mountains, Nevada. *Tectonics*, *29*(6). https://doi.org/10.1029/2009TC002655

Coney, P. J. (1980). Cordilleran metamorphic core complexes: An overview. In M. D. Crittenden, P. J. Coney, & G. H. Davis (Eds.), *Cordilleran metamorphic core complexes* (Vol. 153, pp. 7–34). Geological Society of America Memoir. https://doi.org/10.1130/MEM153

Coney, P. J., & Harms, T. A. (1984). Cordilleran metamorphic core complexes: Cenozoic extensional relics of Mesozoic compression. *Geology*, *12*(9), 550–554. https://doi.org/10.1130/0091-7613(1984)12<550:CMCCCE>2.0.CO;2

Coney, P. J., & Reynolds, S. J. (1977). Cordilleran Benioff zones. *Nature*, *270*(5636), 403–406. https://doi.org/10.1038/270403a0

Constenius, K. N. (1996). Late Paleogene extensional collapse of the Cordilleran foreland fold and thrust belt. *GSA Bulletin*, *108*(1), 20–39. https://doi.org/10.1130/0016-7606(1996)108<0020:lpecot>2.3.co;2

Constenius, K. N., Esse, R. P., & Layer, P. W. (2003). Extensional collapse of the Charleston-Nebo Salient and its relationship to space-time variations in Cordilleran Orogenic Belt tectonismand continental stratigraphy. In R. G. Raynolds, & R. M. Flores (Eds.), *Cenozoic systems of the Rocky Mountain Region Denver* (pp. 303–353). Rocky Mountain SEPM.

Cooper, F. J., Platt, J. P., Anczkiewicz, R., & Whitehouse, M. J. (2010). Footwall dip of a core complex detachment fault: Thermobarometric constraints from the northern Snake Range (Basin and Range, USA). *Journal of Metamorphic Geology*, *28*(9), 997–1020. https://doi.org/10.1111/j.1525-1314.2010.00907.x

Crittenden, M. D., Coney, P. J., & Davis, G. H. (Eds.). (1980). *Cordilleran metamorphic core complexes*. Geological Society of America.

DeCelles, P. G. (2004). Late Jurassic to Eocene evolution of the Cordilleran thrust belt and foreland basin system, western U.S.A. *American Journal of Science*, *304*(2), 105–168. https://doi.org/10.2475/ajs.304.2.105

DeCelles, P. G., & Graham, S. A. (2015). Cyclical processes in the North American Cordilleran orogenic system. *Geology*, *43*(6), 499–502. https://doi.org/10.1130/G36482.1

Desmarais, N. R. (1983). *Geology and geochronology of the Chief Joseph plutonic-metamorphic core complex, Idaho-Montana* (PhD dissertation, p. 125). University of Washington.

Dewey, J. F., & Bird, J. M. (1970). Mountain belts and the new global tectonics. *Journal of Geophysical Research*, *75*(14), 2625–2647. https://doi.org/10.1029/JB075i014p02625

Dickinson, W. R. (2002). The Basin and Range Province as a composite extensional domain. *International Geology Review*, *44*(1), 1–38. https://doi.org/10.2747/0020-6814.44.1.1

Dickinson, W. R., Hopson, C. A., & Saleeby, J. B. (1996). *Alternate origins of the Coast Range Ophiolite (California): Introduction and implications* (p. 10). GSAToday.

Doughty, P. T., Chamberlain, K. R., Foster, D. A., & Sha, G. S. (2007). Structural, metamorphic, and geochronologic constraints on the origin of the Clearwater core complex, northern Idaho. In J. W. Sears, T. A. Harms, & C. A. Evenchick (Eds.), Whence the mountains? Inquiries into the evolution of orogenic systems: A volume in honor of Raymond A. Price. Geological Society of America Special Paper 433. https://doi.org/10.1130/2007.2433(11)

Doughty, P. T., & Price, R. A. (1999). Tectonic evolution of the Priest River complex, northern Idaho and Washington: A reappraisal of the Newport fault with new insights on metamorphic core complex formation. *Tectonics*, *18*(3), 375–393. https://doi.org/10.1029/1998TC900029

du Bray, E. A., Harlan, S. S., & Wilson, A. B. (2006). *Petrology of the crazy mountains dike swarm and geochronology of associated sills, south-central Montana* (U.S. Geological Survey Professional Paper 1714, p. 21).

Ducea, M. N., Triantafyllou, A., & Krcmaric, J. (2020). New timing and depth constraints for the Catalina metamorphic core complex, southeast Arizona. *Tectonics*, *39*(8). https://doi.org/10.1029/2020TC006383

Dudás, F. Ö., Ispolatov, V. O., Harlan, S. S., & Snee, L. W. (2010). Ar geochronology and geochemical reconnaissance of the Eocene Lowland Creek volcanic field, west-central Montana. *The Journal of Geology*, *118*(3), 295–304. https://doi.org/10.1086/651523

Elison, M. W. (1991). Intracontinental contraction in western North America: Continuity and episodicity. *GSA Bulletin*, *103*(9), 1226–1238. https://doi.org/10.1130/0016-7606(1991)103<1226:iciwna>2.3.co;2

Elliott, C. G. (2015). *Geologic map of the Lower Seymour Lake 7.5′ quadrangle, southwestern Montana* (p. 11). Montana Bureau of Mines and Geology Open-File Report 664, 1 sheet, scale 1:24,000.

Elliott, C. G. (2017). *Geologic map of the Lincoln Gulch 7.5′ quadrangle, southwestern Montana*. Montana Bureau of Mines and Geology Geologic Map, 1 sheet, scale 1:24,000.

Emmons, W., & Calkins, F. (1913). *Geology and ore deposits of the Philipsburg quadrangle, Montana*. (Professional Paper No. 78, p. 271).

Engebretson, D. C., Cox, A., & Gordon, R. G. (1985). Relative motions between oceanic and continental plates in the Pacific Basin. *Special Papers—Geological Society of America*, *206*, 59. https://doi.org/10.1130/spe206-p1

Farley, K., Wolf, R., & Silver, L. (1996). The effects of long alpha-stopping distances on (U-Th)/He ages. *Geochimica et Cosmochimica Acta*, *60*(21), 4223–4229. https://doi.org/10.1016/s0016-7037(96)00193-7

Fayon, A. K., Peacock, S. M., Stump, E., & Reynolds, S. J. (2000). Fission track analysis of the footwall of the Catalina detachment fault, Arizona: Tectonic denudation, magmatism, and erosion. *Journal of Geophysical Research*, *105*(B5), 11047–11062. https://doi.org/10.1029/1999JB900421

Feeley, T. C. (2003). Origin and tectonic implications of across-strike geochemical variations in the Eocene Absaroka Volcanic Province, United States. *The Journal of Geology*, *111*(3), 329–346. https://doi.org/10.1086/373972

Feeley, T. C., Cosca, M. A., & Lindsay, C. R. (2002). Petrogenesis and implications of calc-alkaline cryptic hybrid magmas from Washburn volcano, Absaroka Volcanic Province, USA. *Journal of Petrology*, *43*(4), 663–703. https://doi.org/10.1093/petrology/43.4.663

Fitzgerald, P. G., Reynolds, S. J., Stump, E., Foster, D. A., & Gleadow, A. J. W. (1993). Thermochronologic evidence for timing of denudation and rate of crustal extension of the south mountains metamorphic core complex and sierra estrella, Arizona. *Nuclear Tracks and Radiation Measurements*, *21*(4), 555–563. https://doi.org/10.1016/1359-0189(93)90196-G

Flowers, R. M., Ketcham, R. A., Shuster, D. L., & Farley, K. A. (2009). Apatite (U-Th)/He thermochronometry using a radiation damage accumulation and annealing model. *Geochimica et Cosmochimica Acta*, *73*(8), 2347–2365. https://doi.org/10.1016/j.gca.2009.01.015

Foster, D. A., Doughty, P. T., Kalakay, T. J., Fanning, C. M., Coyner, S., Grice, W. C., & Vogl, J. (2007). Kinematics and timing of exhumation of metamorphic core complexes along the Lewis and Clark fault zone, northern Rocky Mountains, USA. In *Special paper 434: Exhumation associated with continental strike-slip fault systems* (Vol. 434, pp. 207–232). Geological Society of America. https://doi.org/10.1130/2007.2434(10)

Foster, D. A., & Fanning, M. C. (1997). Geochronology of the northern Idaho batholith and the Bitterroot metamorphic core complex: Magmatism preceding and contemporaneous with extension. *GSA Bulletin*, *109*(4), 379–394. https://doi.org/10.1130/0016-7606(1997)109<0379:GOTNIB>2.3.CO;2

Foster, D. A., Grice, W. C., & Kalakay, T. J. (2010). Extension of the Anaconda metamorphic core complex: $^{40}Ar/^{39}Ar$ thermochronology and implications for Eocene tectonics of the northern Rocky Mountains and the Boulder batholith. *Lithosphere*, *2*(4), 232–246. https://doi.org/10.1130/L94.1

Foster, D. A., & John, B. E. (1999). Quantifying tectonic exhumation in an extensional orogen with thermochronology: Examples from the southern Basin and Range Province. *Geological Society, London, Special Publications*, *154*(1), 343–364. https://doi.org/10.1144/GSL.SP.1999.154.01.16

Foster, D. A., Mueller, P. A., Heatherington, A., Gifford, J. N., & Kalakay, T. J. (2012). Lu–Hf systematics of magmatic zircons reveal a Proterozoic crustal boundary under the Cretaceous Pioneer batholith, Montana. *Lithos*, *142–143*, 216–225. https://doi.org/10.1016/j.lithos.2012.03.005

Foster, D. A., & Raza, A. (2002). Low-temperature thermochronological record of exhumation of the Bitterroot metamorphic core complex, northern Cordilleran Orogen. *Tectonophysics*, *349*(1–4), 23–36. https://doi.org/10.1016/S0040-1951(02)00044-6

Foster, D. A., Schafer, C., Fanning, C. M., & Hyndman, D. W. (2001). Relationships between crustal partial melting, plutonism, orogeny, and exhumation: Idaho–Bitterroot batholith. *Tectonophysics*, *342*(3–4), 313–350. https://doi.org/10.1016/S0040-1951(01)00169-X

Fritz, W. J., Sears, J. W., McDowell, R. J., & Wampler, J. M. (2007). Cenozoic volcanic rocks of southwestern Montana. *Northwest Geology*, *36*, 91–110.

Fuston, S., & Wu, J. (2020). Raising the Resurrection plate from an unfolded-slab plate tectonic reconstruction of northwestern North America since early Cenozoic time. *GSA Bulletin*, *133*, 1–13. https://doi.org/10.1130/B35677.1

Gans, P. B., & Bohrson, W. A. (1998). Suppression of volcanism during rapid extension in the Basin and Range Province, United States. *Science*, *279*(5347), 66–68. https://doi.org/10.1126/science.279.5347.66

Gans, P. B., & Gentry, B. J. (2016). Dike emplacement, footwall rotation, and the transition from magmatic to tectonic extension in the Whipple Mountains metamorphic core complex, southeastern California: Dike Emplacement and Footwall Rotation. *Tectonics*, *35*(11), 2564–2608. https://doi.org/10.1002/2016TC004215

Gans, P. B., Mahood, G. A., & Schermer, E. (1989). *Synextensional magmatism in the Basin and Range Province: A case study from the eastern Great Basin* (Vol. 233, p. 53). Geological Society of America.

Gaschnig, R. M., Vervoort, J. D., Lewis, R. S., & Tikoff, B. (2011). Isotopic evolution of the Idaho Batholith and Challis Intrusive Province, Northern US Cordillera. *Journal of Petrology*, *52*(12), 2397–2429. https://doi.org/10.1093/petrology/egr050

Gehrels, G., & Pecha, M. (2014). Detrital zircon U-Pb geochronology and Hf isotope geochemistry of Paleozoic and Triassic passive margin strata of western North America. *Geosphere*, *10*(1), 49–65. https://doi.org/10.1130/GES00889.1

Gehrels, G., Rusmore, M., Woodsworth, G., Crawford, M., Andronicos, C., Hollister, L., et al. (2009). U-Th-Pb geochronology of the Coast Mountains batholith in north-coastal British Columbia: Constraints on age and tectonic evolution. *Geological Society of America Bulletin*, *121*(9–10), 1341–1361. https://doi.org/10.1130/B26404.1

Gottardi, R., McAleer, R., Casale, G., Borel, M., Iriondo, A., & Jepson, G. (2020). Exhumation of the Coyote Mountains metamorphic core complex (Arizona): Implications for orogenic collapse of the Southern North American Cordillera. *Tectonics*, *39*(8). https://doi.org/10.1029/2019TC006050

Gottardi, R., Schaper, M. C., Barnes, J. D., & Heizler, M. T. (2018). Fluid–rock interaction and strain localization in the Picacho Mountains detachment shear zone, Arizona, USA. *Tectonics*, *37*(9), 3244–3260. https://doi.org/10.1029/2017TC004835

Green, P., Duddy, I., Gleadow, A., Tingate, P., & Laslett, G. (1986). Thermal annealing of fission tracks in apatite: 1. A qualitative description. *Chemical Geology: Isotope Geoscience section*, *59*(4), 237–253. https://doi.org/10.1016/0168-9622(86)90074-6

Grice, W. C. (2006). *Exhumation and cooling history of the Middle Eocene Anaconda metamorphic core complex, western Montana* (M.S. thesis, p. 276). University of Florida.

Grove, M., & Harrison, T. M. (1996). ^{40}Ar diffusion in Fe-rich biotite. *American Mineralogist*, *81*(7–8), 940–951. https://doi.org/10.2138/am-1996-7-816

Guenthner, W. R., Reiners, P. W., Ketcham, R. A., Nasdala, L., & Giester, G. (2013). Helium diffusion in natural zircon: Radiation damage, anisotropy, and the interpretation of zircon (U-Th)/He thermochronology. *American Journal of Science*, *313*(3), 145–198. https://doi.org/10.2475/03.2013.01

Hamilton, W. B. (1969). Mesozoic California and the underflow of the Pacific mantle. *Geological Society of America Bulletin*, *80*, 2409–2430. https://doi.org/10.1130/0016-7606(1969)80[2409:mcatuo]2.0.co;2

Hill, E. J., Baldwin, S. L., & Lister, G. S. (1995). Magmatism as an essential driving force for formation of active metamorphic core complexes in eastern Papua New Guinea. *Journal of Geophysical Research*, *100*(B6), 10441–10451. https://doi.org/10.1029/94JB03329

Hourigan, J., Reiners, P., & Brandon, M. (2005). U/Th zonation-dependent alpha-ejection in (U-Th)/He chronometry. *Geochimica et Cosmochimica Acta*, *69*(13), 3349–3365. https://doi.org/10.1016/j.gca.2005.01.024

House, M. A., Bowring, S. A., & Hodges, K. V. (2002). Implications of middle Eocene epizonal plutonism for the unroofing history of the Bitterroot metamorphic core complex, Idaho-Montana. *GSA Bulletin*, *114*(4), 448–461. https://doi.org/10.1130/0016-7606(2002)114<0448:IOMEEP>2.0.CO;2

Howlett, C. J., & Laskowski, A. K. (2021). Determining the source of placer gold in the Anaconda metamorphic core complex supradetachment basin using detrital zircon U-Pb geochronology, western Montana, USA. *Geosphere*, *17*(1), 154–170. https://doi.org/10.1130/GES02226.1

Howlett, C. J., Reynolds, A. N., & Laskowski, A. K. (2020). *Geologic map of the northern half of the Pintler Lake 7.5′ quadrangle and the southern half of the Warren Peak 7.5′ quadrangle, southwestern Montana*. Montana Bureau of Mines and Geology EDMAP portion of the National Geologic Mapping Program 13, 1 sheet, scale 1:24,000.

Humphreys, E. D. (1995). Post-Laramide removal of the Farallon slab, western United States. *Geology*, *23*(11), 987–990. https://doi.org/10.1130/0091-7613(1995)023<0987:plrotf>2.3.co;2

Humphreys, E. D. (2009). Relation of flat subduction to magmatism and deformation in the western United States. In S. M. Kay, V. A. Ramos, & W. R. Dickinson (Eds.), *Backbone of the Americas: Shallow subduction, plateau uplift, and ridge and terrane collision* (Geological Society of America Memoir 204, pp. 1–14). https://doi.org/10.1130/2009.1204(04)

Humphreys, E. D., Hessler, E., Dueker, K., Farmer, G. L., Erslev, E., & Atwater, T. (2003). How Laramide-age hydration of North American lithosphere by the farallon slab controlled subsequent activity in the western United States. *International Geology Review*, *45*(7), 575–595. https://doi.org/10.2747/0020-6814.45.7.575

Ispolatov, V. O. (1997). *^{40}Ar/^{39}Ar geochronology of the Lowland Creek volcanic field and its temporal relations with the other Eocene volcanic areas* (M.S. thesis, p. 105). Old Dominion University.

Kalakay, T. J., Foster, D. A., & Thomas, R. A. (2003). Geometry, kinematics and timing of extension in the Anaconda extensional terrane, western Montana. *Northwest Geology*, *32*, 124–133.

Ketcham, R. A. (2005). Forward and inverse modeling of low-temperature thermochronometry data. *Reviews in Mineralogy and Geochemistry*, *58*(1), 275–314. https://doi.org/10.2138/rmg.2005.58.11

Kincaid, C., & Olson, P. (1987). An experimental study of subduction and slab migration. *Journal of Geophysical Research*, *92*(B13), 13832–13840. https://doi.org/10.1029/JB092iB13p13832

Konstantinou, A., Strickland, A., Miller, E., Vervoort, J., Fisher, C. M., Wooden, J., & Valley, J. (2013). Synextensional magmatism leading to crustal flow in the Albion-Raft River-Grouse Creek metamorphic core complex, northeastern Basin and Range: Synextensional magmatism in the ARG. *Tectonics*, *32*(5), 1384–1403. https://doi.org/10.1002/tect.20085

Konstantinou, A., Strickland, A., Miller, E. L., & Wooden, J. P. (2012). Multistage Cenozoic extension of the Albion–Raft River–Grouse Creek metamorphic core complex: Geochronologic and stratigraphic constraints. *Geosphere*, *8*(6), 1429–1466. https://doi.org/10.1130/GES00778.1

Kruckenberg, S. C., Whitney, D. L., Teyssier, C., Fanning, C. M., & Dunlap, W. J. (2008). Paleocene-Eocene migmatite crystallization, extension, and exhumation in the hinterland of the northern Cordillera: Okanogan dome, Washington, USA. *Geological Society of America Bulletin*, *120*(7–8), 912–929. https://doi.org/10.1130/B26153.1

Lageson, D. R., Schmitt, J. G., Horton, B. K., Kalakay, T. J., & Burton, B. R. (2001). Influence of Late Cretaceous magmatism on the Sevier orogenic wedge, western Montana. *Geology*, *29*(8), 723–726. https://doi.org/10.1130/0091-7613(2001)029<0723:iolcmo>2.0.co;2

Lee, J., Blackburn, T., & Johnston, S. (2017). Timing of mid-crustal ductile extension in the northern Snake Range metamorphic core complex, Nevada: Evidence from U/Pb zircon ages. *Geosphere*, *13*(2), 439–459. https://doi.org/10.1130/GES01429.1

Lin, S., Jiang, D., & Williams, P. F. (2007). Importance of differentiating ductile slickenside striations from stretching lineations and variation of shear direction across a high-strain zone. *Journal of Structural Geology*, *29*(5), 850–862. https://doi.org/10.1016/j.jsg.2006.12.006

Lipman, P. W., Prostka, H. J., & Christiansen, R. L. (1971). Evolving subduction zones in the western United States, as interpreted from igneous rocks. *Science*, *174*(4011), 821–825. https://doi.org/10.1126/science.174.4011.821

Lister, G. S., & Baldwin, S. L. (1993). Plutonism and the origin of metamorphic core complexes. *Geology*, *21*, 607–610. https://doi.org/10.1130/0091-7613(1993)021<0607:patoom>2.3.co;2

Liu, M. (2001). Cenozoic extension and magmatism in the North American Cordillera: The role of gravitational collapse. *Tectonophysics*, *342*(3–4), 407–433. https://doi.org/10.1016/S0040-1951(01)00173-1

Loen, J. S. (1994). Origin of placer gold nuggets and history of formation of glacial gold placers, Gold Creek, Granite County, Montana. *Economic Geology*, *89*(1), 91–104. https://doi.org/10.2113/gsecongeo.89.1.91

Lonn, J. D., McDonald, C., Lewis, R. S., Kalakay, T. J., O'Neill, J. M., Berg, R. B., & Hargrave, P. (2003). *Preliminary geologic map of the Philipsburg 30′ × 60′ quadrangle, western Montana*. Montana Bureau of Mines and Geology Open-File Report MBMG 483, scale 1:100,000.

Lorencak, M., Seward, D., Vanderhaeghe, O., Teyssier, C., & Burg, J. P. (2001). Low-temperature cooling history of the Shuswap metamorphic core complex, British Columbia; constraints from apatite and zircon fission-track ages. *Canadian Journal of Earth Sciences*, *38*(11), 1615–1625. https://doi.org/10.1139/e01-037

MacCready, T., Snoke, A. W., Wright, J. E., & Howard, K. A. (1997). Mid-crustal flow during Tertiary extension in the Ruby Mountains core complex, Nevada. *GSA Bulletin*, *109*(12), 1576–1594. https://doi.org/10.1130/0016-7606(1997)109<1576:MCFDTE>2.3.CO;2

Madsen, J. K., Thorkelson, D. J., Friedman, R. M., & Marshall, D. D. (2006). Cenozoic to recent plate configurations in the Pacific Basin: Ridge subduction and slab window magmatism in western North America. *Geosphere*, *2*(1), 11–34. https://doi.org/10.1130/GES00020.1

McDougall, I., & Harrison, T. (1999). *Geochronology and thermochronology by the $^{40}Ar/^{39}Ar$ method* (2nd ed.). Oxford University Press.

McKervey, J. A. (1998). *The petrogenesis of the Eocene Challis volcanic Group*. https://doi.org/10.21954/OU.RO.0000E215

Miller, E. L., Dumitru, T. A., & Brown, R. W. (1999). Rapid Miocene slip on the Snake Range–Deep Creek Range fault system, east-central Nevada. *Geological Society of America Bulletin*, *111*, 886–905.

Miller, E. L., Gans, P. B., Wright, J. E., & Sutter, J. F. (1988). Metamorphic history of the east-central Basin and Range Province: Tectonic setting and relationship to magmatism. In W. G. Ernst (Ed.), *Metamorphism and crustal evolution of the western United States* (Rubey volume VII, pp. 649–682). Prentice-Hall.

Morris, G. A., Larson, P. B., & Hooper, P. R. (2000). 'Subduction style' magmatism in a non-subduction setting: The Colville Igneous Complex, NE Washington State, USA. *Journal of Petrology*, *41*(1), 43–67. https://doi.org/10.1093/petrology/41.1.43

Mueller, C. (2019). *Thermochronology of the deep crust in the northern Ruby Mountains, NV* (B.S. thesis, p. 30). University of Colorado.

Mulcahy, S. R., Starnes, J. K., Day, H. W., Coble, M. A., & Vervoort, J. D. (2018). Early onset of Franciscan subduction. *Tectonics*, *37*(5), 1194–1209. https://doi.org/10.1029/2017TC004753

Norman, M. D., & Mertzman, S. A. (1991). Petrogenesis of Challis volcanics from central and southwestern Idaho: Trace element and Pb isotopic evidence. *Journal of Geophysical Research*, *96*(B8), 13279–13293. https://doi.org/10.1029/91JB00285

O'Neill, J. M., Lonn, J. D., Lageson, D. R., & Kunk, M. J. (2004). Early tertiary Anaconda metamorphic core complex, southwestern Montana. *Canadian Journal of Earth Sciences*, *41*(1), 63–72. https://doi.org/10.1139/e03-086

Parsons, T., & Thompson, G. A. (1993). Does magmatism influence low-angle normal faulting? *Geology*, *21*(3), 247–250. https://doi.org/10.1130/0091-7613(1993)021<0247:DMILAN>2.3.CO;2

Paterson, S. R., Vernon, R. H., & Tobisch, O. T. (1989). A review of criteria for the identification of magmatic and tectonic foliations in granitoids. *Journal of Structural Geology*, *11*(3), 349–363. https://doi.org/10.1016/0191-8141(89)90074-6

Platt, J. P., Behr, W. M., & Cooper, F. J. (2015). Metamorphic core complexes: Windows into the mechanics and rheology of the crust. *Journal of the Geological Society*, *172*(1), 9–27. https://doi.org/10.1144/jgs2014-036

Prior, M. G., Stockli, D. F., & Singleton, J. S. (2016). Miocene slip history of the Eagle Eye detachment fault, Harquahala Mountains metamorphic core complex, west-central Arizona. *Tectonics*, *35*(8), 1913–1934. https://doi.org/10.1002/2016TC004241

Reiners, P., Spell, T., Nicolescu, S., & Zanetti, K. (2004). Zircon (U-Th)/He thermochronometry: He diffusion and comparisons with $^{40}Ar/^{39}Ar$ dating. *Geochimica et Cosmochimica Acta*, *68*(8), 1857–1887. https://doi.org/10.1016/j.gca.2003.10.021

Reynolds, S. J., Shafiqullah, M., Damon, P. E., & DeWitt, E. (1986). Early miocene mylonitization and detachment faulting, South Mountains, Central Arizona. *Geology*, *14*(4), 283. https://doi.org/10.1130/0091-7613(1986)14<283:EMMADF>2.0.CO;2

Richard, S. M., Fryxell, J. E., & Sutter, J. F. (1990). Tertiary structure and thermal history of the Harquahala and Buckskin Mountains, west central Arizona: Implications for denudation by a major detachment fault system. *Journal of Geophysical Research*, *95*(B12), 19973. https://doi.org/10.1029/JB095iB12p19973

Roe, W. P. (2010). *Tertiary sediments of the Big Hole Valley and Pioneer Mountains, southwestern Montana: Age, provenance, and tectonic implications* (M.S. thesis, p. 117). University of Montana.

Schmandt, B., & Humphreys, E. (2011). Seismically imaged relict slab from the 55 Ma Siletzia accretion to the northwest United States. *Geology*, *39*(2), 175–178. https://doi.org/10.1130/G31558.1

Scott, R. J., Foster, D. A., & Lister, G. S. (1998). Tectonic implications of rapid cooling of lower plate rocks from the Buckskin-Rawhide metamorphic core complex, west-central Arizona. *Geological Society of America Bulletin*, *110*(5), 588–614. https://doi.org/10.1130/0016-7606(1998)110<0588:tiorco>2.3.co;2

Sears, J. W., & Hendrix, M. S. (2004). Lewis and Clark line and the rotational origin of the Alberta and Helena salients, North American Cordillera. In *Special paper 383: Orogenic curvature: Integrating paleomagnetic and structural analyses* (Vol. 383, pp. 173–186). Geological Society of America. https://doi.org/10.1130/0-8137-2383-3(2004)383[173:LACLAT]2.0.CO;2

Sengör, A. M. C., & Burke, K. (1978). Relative timing of rifting and volcanism on Earth and its tectonic implications. *Geophysical Research Letters*, *5*(6), 419–421. https://doi.org/10.1029/GL005i006p00419

Severinghaus, J., & Atwater, T. (1990). Cenozoic geometry and thermal state of the subducting slabs beneath western North America. *Geological Society of America Memoirs*, *176*, 1–22. https://doi.org/10.1130/MEM176-p1

Sharman, G. R., Sharman, J. P., & Sylvester, Z. (2018). detritalPy: A Python-based toolset for visualizing and analysing detrital geo-thermochronologic data. *The Depositional Record*, *4*, 202–215. https://doi.org/10.1002/dep2.45

Silverberg, D. S. (1990). *The tectonic evolution of the Pioneer metamorphic core complex, south-central Idaho* (PhD thesis, p. 282). Department of Earth, Atmospheric, and Planetary Sciences, Massachusetts Institute of Technology.

Singleton, J. S., Stockli, D. F., Gans, P. B., & Prior, M. G. (2014). Timing, rate, and magnitude of slip on the Buckskin-Rawhide detachment fault, west central Arizona. *Tectonics*, *33*(8), 1596–1615. https://doi.org/10.1002/2013TC003517

Snoke, A. W., Howard, K. A., McGrew, A. J., Burton, B. R., Barnes, C. G., Peters, M. T., & Wright, J. E. (1997). The grand tour of the Ruby-East Humboldt metamorphic core complex, northeastern Nevada: Part 1—Introduction & road log. *Brigham Young University Geology Studies*, *42*(1), 225–296.

Spencer, J. E., & Reynolds, S. J. (1990). Relationship between Mesozoic and Cenozoic tectonic features in west central Arizona and adjacent southeastern California. *Journal of Geophysical Research*, *95*(B1), 539. https://doi.org/10.1029/JB095iB01p00539

Spencer, J. E., Richard, S. M., Reynolds, S. J., Miller, R. J., Shafiqullah, M., Gilbert, W. G., & Grubensky, M. J. (1995). Spatial and temporal relationships between mid-Tertiary magmatism and extension in southwestern Arizona. *Journal of Geophysical Research*, *100*(B6), 10321–10351. https://doi.org/10.1029/94JB02817

Stevens, L. M., Baldwin, J. A., Crowley, J. L., Fisher, C. M., & Vervoort, J. D. (2016). Magmatism as a response to exhumation of the Priest River complex, northern Idaho: Constraints from zircon U–Pb geochronology and Hf isotopes. *Lithos*, *262*, 285–297. https://doi.org/10.1016/j.lithos.2016.07.006

Stevens, L. M., Bendick, R., & Baldwin, J. A. (2017). Synconvergent exhumation of metamorphic core complexes in the northern North American Cordillera. *Geology*, *45*(6), 495–498. https://doi.org/10.1130/G38802.1

Stockli, D. F., Brichau, S., Dewane, T. J., Hager, C., & Schroeder, J. (2006). Dynamics of large-magnitude extension in the Whipple Mountains metamorphic core complex. *Geochimica et Cosmochimica Acta*, *70*, A616. https://doi.org/10.1016/j.gca.2006.06.1143

Tao, W. C., & O'Connell, R. J. (1992). Ablative subduction: A two-sided alternative to the conventional subduction model. *Journal of Geophysical Research*, *97*(B6), 8877. https://doi.org/10.1029/91JB02422

Terrien, J. (2012). *Thermochronological and geochemical insights on the transition between the metamorphic core complex and the North American Cordillera, southern Arizona* (PhD dissertation, p. 245). Syracuse University.

van der Pluijm, B. A., Vrolijk, P. J., Pevear, D. R., Hall, C. M., & Solum, J. (2006). Fault dating in the Canadian Rocky Mountains: Evidence for late Cretaceous and early Eocene orogenic pulses. *Geology*, *34*(10), 837. https://doi.org/10.1130/G22610.1

Vanderhaeghe, O., & Teyssier, C. (2001). Crustal-scale rheological transitions during late-orogenic collapse. *Tectonophysics*, *335*(1–2), 211–228. https://doi.org/10.1016/S0040-1951(01)00053-1

Vanderhaeghe, O., Teyssier, C., McDougall, I., & Dunlap, W. J. (2003). Cooling and exhumation of the Shuswap metamorphic core complex constrained by $^{40}Ar/^{39}Ar$ thermochronology. *GSA Bulletin*, *115*(2), 200–216. https://doi.org/10.1130/0016-7606(2003)115<0200:caeots>2.0.co;2

Vervoort, J. D. (2014). Lu-Hf dating: The Lu-Hf isotope system. In W. J. Rink, & J. Thompson (Eds.), *Encyclopedia of scientific dating methods* (pp. 1–20). Springer Netherlands. https://doi.org/10.1007/978-94-007-6326-5_46-1

Vervoort, J. D., Patchett, P. J., Blichert-Toft, J., & Albarède, F. (1999). Relationships between Lu–Hf and Sm–Nd isotopic systems in the global sedimentary system. *Earth and Planetary Science Letters*, *168*(1–2), 79–99. https://doi.org/10.1016/S0012-821X(99)00047-3

Vogl, J. J., Foster, D. A., Fanning, C. M., Kent, K. A., Rodgers, D. W., & Diedesch, T. (2012). Timing of extension in the Pioneer metamorphic core complex with implications for the spatial-temporal pattern of Cenozoic extension and exhumation in the northern U.S. Cordillera: Extension in the Pioneer core complex. *Tectonics*, *31*(1). https://doi.org/10.1029/2011TC002981

Wallace, C. A., Lidke, D. J., Elliott, J. E., Desmarais, N. R., Obradovich, J. D., Lopez, D. A., et al. (1992). *Geologic map of the Anaconda-Pintlar wilderness and contiguous roadless area, Granite, Deer Lodge, Beaverhead, and Ravalli counties, western Montana*. U.S. Geological Survey Miscellaneous Field Studies Map MF-1633-C, scale 1:50,000.

Wells, M. L., & Hoisch, T. D. (2008). The role of mantle delamination in widespread Late Cretaceous extension and magmatism in the Cordilleran orogen, western United States. *Geological Society of America Bulletin*, *120*(5–6), 515–530. https://doi.org/10.1130/B26006.1

Wells, M. L., Snee, L. W., & Blythe, A. E. (2000). Dating of major normal fault systems using thermochronology: An example from the Raft River detachment, Basin and Range, western United States. *Journal of Geophysical Research*, *105*(B7), 16303–16327. https://doi.org/10.1029/2000JB900094

Wells, R. E., Bukry, D., Friedman, R., Pyle, D., Duncan, R., Haeussler, P., & Wooden, J. (2014). Geologic history of Siletzia, a large igneous province in the Oregon and Washington Coast Range: Correlation to the geomagnetic polarity time scale and implications for a long-lived Yellowstone hotspot. *Geosphere*, *10*(4), 692–719. https://doi.org/10.1130/GES01018.1

Wells, R. E., Engebretson, D. C., Snavely, P. D., & Coe, R. S. (1984). Cenozoic plate motions and the volcano-tectonic evolution of western Oregon and Washington. *Tectonics*, *3*(2), 275–294. https://doi.org/10.1029/TC003i002p00275

Wernicke, B. P. (1981). Low-angle normal faults in the Basin and Range Province: Nappe tectonics in an extending orogen. *Nature*, *291*(5817), 645–648. https://doi.org/10.1038/291645a0

Wernicke, B. P. (1992). Cenozoic extensional tectonics of the U.S. Cordillera. In B. C. Burchfiel, P. W. Lipman, & M. L. Zoback (Eds.), *The Cordilleran orogen* (pp. 553–582). Geological Society of America. https://doi.org/10.1130/DNAG-GNA-G3.553

Wernicke, B. P., England, P. C., Sonder, L. J., & Christiansen, R. L. (1987). Tectonomagmatic evolution of Cenozoic extension in the North American Cordillera. *Geological Society, London, Special Publications*, *28*(1), 203–221. https://doi.org/10.1144/GSL.SP.1987.028.01.15

Whitney, D. L., Teyssier, C., Rey, P., & Buck, W. R. (2013). Continental and oceanic core complexes. *Geological Society of America Bulletin*, *125*(3–4), 273–298. https://doi.org/10.1130/B30754.1

Whitney, D. L., Teyssier, C., & Vanderhaeghe, O. (2004). Gneiss domes and crustal flow. In D. L. Whitney, C. Teyssier, & C. S. Siddoway (Eds.), *Gneiss domes in orogeny*. Geological Society of America. https://doi.org/10.1130/0-8137-2380-9.15

Wong, M. S., & Gans, P. B. (2008). Geologic, structural, and thermochronologic constraints on the tectonic evolution of the Sierra Mazatán core complex, Sonora, Mexico: New insights into metamorphic core complex formation. *Tectonics*, *27*(4), 1–31. https://doi.org/10.1029/2007tc002173

Wong, M. S., Gans, P. B., & Scheier, J. (2010). $^{40}Ar/^{39}Ar$ thermochronology of core complexes and other basement rocks in Sonora, Mexico: Implications for Cenozoic tectonic evolution of northwestern Mexico. *Journal of Geophysical Research*, *115*(B7), B07414. https://doi.org/10.1029/2009JB007032

Yonkee, W. A., & Weil, A. B. (2015). Tectonic evolution of the Sevier and Laramide belts within the North American Cordillera orogenic system. *Earth-Science Reviews*, *150*, 531–593. https://doi.org/10.1016/j.earscirev.2015.08.001

Reference From the Supporting Information

Reynolds, A. N., Howlett, C. J., & Laskowski, A. K. (2019). *Extension of the Anaconda metamorphic core complex: Low-temperature thermochronology from the footwall of the Anaconda detachment, southwest Montana* (p. 335709). GSA Annual Meeting. https://doi.org/10.1130/abs/2019AM-335709